Elucidating the impact of charge selective contact in halide perovskite through impedance spectroscopy

Mohd Taukeer Khan [a,c], *Manuel Salado* [a], *Abdullah Almohammedi* [c] *Samrana Kazim,* [a,b] *and Shahzada Ahmad,* [a,b*]

[a] BCMaterials-Basque Center for Materials, Applications and Nanostructures, Martina Casiano, UPV/EHU Science Park, Barrio Sarriena s/n, Leioa 48940, Spain.

[b] IKERBASQUE, Basque Foundation for Science, Bilbao, 48013, Spain.

[c] Department of Physics, Faculty of Science, Islamic University of Madinah, Prince Naifbin Abdulaziz, Al Jamiah, Madinah 42351, Kingdom of Saudi Arabia.
Tel: +34 946128811 Email: shahzada.ahmad@bcmaterials.net

Abstract

The electron and hole selective contact (SC) play a pivotal role in the performance of perovskite solar cells. In order to separate the interfacial phenomenon from bulk, the influence of charge SC was elucidated, by means of impedance spectroscopy. The specific role played by TiO_2 and *Spiro-OMeTAD* as electron and hole SC in perovskite solar cells was investigated at short circuit condition at different temperatures. We have probed $MAPbI_3$ and $(FAPbI_3)_{0.85}(MAPbBr_3)_{0.15}$ and elucidated parameters such as charge carrier mobility, recombination resistance, time constant and charge carrier kinetics in perovskite layer and at the interface of perovskite/SC. Charge carrier mobility in mixed perovskite was found to be nearly two order of magnitude higher as compared to $MAPbI_3$. Moreover, the carrier mobility in devices with only electron SC was found to be higher as compared only hole SC. The charge accumulation at TiO_2/perovskite/*Spiro*-OMeTAD interfaces were studied via frequency dependent capacitance, revealing higher charge accumulation at perovskite/S*piro*-OMeTAD than at TiO_2/perovskite interface. By performing varying temperature frequency dependent capacitance measurements the distribution of density of state within the bandgap of the perovskites, the emission rate of electrons from the trap states and traps activation energy was determined.

Keywords: electron selective contact; hole selective contact; density of state; charge carrier mobility; impedance spectroscopy.

Introduction

The field of perovskite solar cells was initiated by the use of model MAPbI$_3$, and its success paved the way for new formulations by the means of compositional engineering of perovskites.[1] Tweaking of halide anion and/or organic cation allowed to push the efficiency as well as stability.[2] Power conversion efficiencies as high as 25.2% have been reported at laboratory scale[3], which is on par with other matured thin film PV technologies. The realization of perovskite for solar cells application was due to its intriguing opto-electrical properties, which led, to its exploitation in other opto-electrical devices such as lasing,[4] X-ray, OLEDs,[5] and photodiodes.[6] Despite its unparalleled performance, the perovskites solar cells suffer from several key issues such as anomalous *J-V* hysteresis, electrical instability, non-radiative recombination losses, and environmental instability. The primary cause for *J-V* hysteresis are intrinsic defects present in the perovskites layers and charge accumulation at interfaces.[7–10] The plausible reason for the charge accumulation at the interface can be unbalanced electron and hole mobility which allows charge to be accumulated at the perovskite/electron selective contact (ESC) and perovskite/hole selective contact (HSC) interface.[11]

In the past we have reported unbalance charge extraction along with its charge injection time scale and also noted charge accumulation at ESC/perovskite interface.[12] The defect states present in the bulk of perovskite effect the charge accumulation near the interface. Furthermore, the presence of defects in the bulk of perovskites further act as trapping center for charge carriers, which in turn cause non-radiative losses and decreases charge carrier's lifetimes leading to deterioration in the device performance. Moreover, the presence of inorganic part suggest mixed conductivity, with contribution from both electronic and ionic conductivity. The ion migration was also speculated to be one of the reason for low long term photovoltaic behavior under stress condition or at V_{oc}.[13,14] Similarly cathode materials such as silver or gold was reported to be found at anode side, which travelled all the way through hole transport materials and perovskites. This diffusion of metallic contact into the active material is a loss, and this process can activate intensely by thermal process.[15] Apart from all these, the undesirable process in which dopant ions mainly Li$^+$ (used in HSC) can diffuses into perovskite matrix and destabilized the stoichiometry due to its hydrophillicity.[16] Despite the numerous studies reported in the literature, the meticulous device physics and role of ESC and HSC in perovskite solar cells are still ambiguous. Consequently, for the assessment and understanding of selective contacts and electrical parameters of device needs

to be investigated to unravel the charge kinetics, will allow perovskites solar cells for further optimization.

Impedance spectroscopy is a sensitive technique, which can be utilized to probe the dynamic electrical properties occurring inside the perovskite solar cells. It can provide the information about the various resistive and capacitive process such as charge transport, recombination losses, interfacial charge accumulation etc. Due to a large variety of equivalent circuits available in literature and overlapping of various capacitive process e.g. overlapping of accumulation and geometrical capacitance at intermediate frequencies, the interpretation of the derived fitted parameters are still obscure. Herein, to elucidate the underlying various electrical and physical process which control the PV performance, we have selected two standard organohalide perovskites [MAPbI$_3$ and (FAPbI$_3$)$_{0.85}$(MAPbBr$_3$)$_{0.15}$]. In order to separate the interfacial and bulk related process and decode the role of each SC for solar cells, the devices with and without selective contact was also probed. Photo-induced carriers change the polarizability of perovskite layer which allows three orders of increment in low frequency dielectric constant of MAPbI$_3$.[17] Moreover, illumination also leads to a uniform lattice expansion in perovskite which can further modify the electrical properties.[18] Besides, the ferroelectric nature of MAPbI$_3$ is also influenced by charge injection at applied bias due to build-up ion-induced structural fluctuations and polarization.[19,20] To avoid such phenomena, we have performed the measurements in dark and at short circuit (i.e. no DC bias) condition. The configuration of each device is represented in Table 1 along with the classification of the type of structure used for both perovskite, and the schematics of the devices are shown in Figure 1.

Table 1. Device configurations of MAPbI$_3$ and (FAPbI$_3$)$_{0.85}$(MAPbBr$_3$)$_{0.15}$ perovskites.

MAPbI$_3$		Type of structure	(FAPbI$_3$)$_{0.85}$(MAPbBr$_3$)$_{0.15}$	
FTO/MAPbI$_3$/Au	Type A	only perovskite	FTO/mix-Pero/Au	A´
FTO/ MAPbI$_3$/HTM/Au	Type B	perovskite with HTM	FTO/mix-Pero/HTM /Au	B´
FTO/c-TiO$_2$/ m-TiO$_2$/ MAPbI$_3$/ Au	Type C	perovskite with ETM	FTO/ c-TiO$_2$/ m-TiO$_2$/mix-Pero/Au	C´
FTO/ c-TiO$_2$/ m-TiO$_2$/ MAPbI$_3$/HTM/Au	Type D	Full device	FTO/ c-TiO$_2$/m-TiO$_2$/mix-Pero/HTM/Au	D´
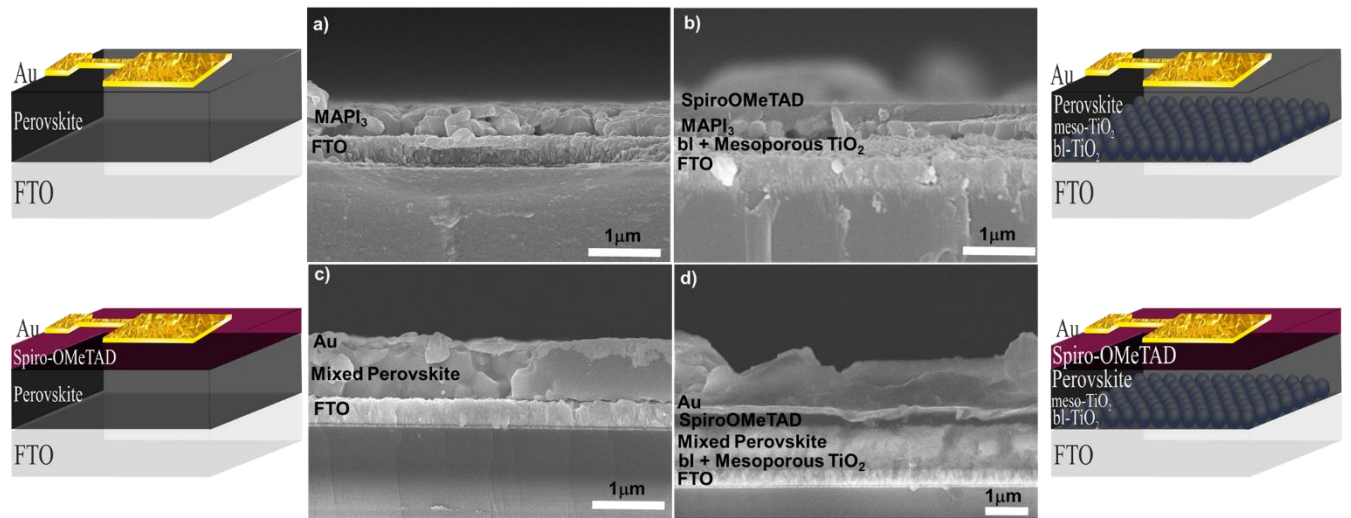
Figure 1. Cross sectional SEM for (a) device 1, Type A (b) device 4, Type D (c) device 5, Type A'
and (d) device, Type D'. Here, bl refers to TiO$_2$ blocking layer.


Results and discussions

Figure 1 shows the cross-sectional view of scanning electron micrograph for fabricated devices to
gaze the thickness of different layers. The type of architect used can be deducted from the
micrographs.

The role of TiO$_2$ (compact + mesoporous) and *Spiro*-OMeTAD as electron and hole SC on charge
transfer and recombination process inside the perovskite solar cells was systematically analyzed
via impedance spectroscopy. Figure 2a-d and Figure 3a-d display the impedance arch for full
device or without selective contact in the temperature range 300 – 360 K. We noted the appearance
of semicircle and the radius of semicircle decreases with an increase in temperature for all curves.
It can be deducted from Figures that the full device (type D & D´) has high resistance whereas the
devices without any charge extraction layers (type A and & A´) showed least resistance. From
Figure 2b and 2c, it can be concluded that the main resistive component in device is due to ESC
(*i.e.* TiO$_2$). The measurements based on MAPbI$_3$, and without selective contact (type A, B, C)
display a single semicircle, whereas the full device fabricated from MAPbI$_3$ (Type D) showed two
semicircles at higher temperature (>330 K), attributed to the double relaxation behavior, one at the
interface, while the other in bulk of perovskite. The semicircle at higher frequency (HF) is
associated to the charge transfer and recombination through perovskite/charge selective contacts
mainly perovskite/*Spiro*-OMeTAD interfaces, [46, 53, 54] and the semicircle at low frequency (LF)

4

attributed to charge carrier (e-h) recombination, dielectric relaxation, and ionic migration in perovskite layer.[21, 46, 53, 55-57] The HF part is missing for devices without SC (type A & A´), plausibly the interfacial recombination process in such devices is fast enough and it did not showed in the measured frequency range (2 MHz). We have noted, the selective contact play an important role to minimize the interfacial recombination. The LF arc in the impedance spectra (IS) of devices based on mixed cations (except device type A´) is clearly visible as compared to MAPbI$_3$ devices. This implies that, the ionic migration and dielectric relaxation in MAPbI$_3$ perovskites is slow enough to show its signature in the LF region while in case of mixed perovskite these effects are more prominent than MAPbI$_3$.

The equivalent circuit shown in Figure 2e-f and Figure 3e-g were used to model the experimental impedance results of each devices. Each circuit represents a series resistance R$_1$ ascribed to the contact resistance of electrical wire and fluorine doped tin oxide (FTO) based electrode which was deduced from high frequency intercept on the real-axis.[22–24] The value of R$_1$ used to model the IS are given in supporting information (SI) and are in the range of $7 - 20\ \Omega$. The LF part of the IS was modeled using Ist RC element shown in equivalent circuit, where R$_2$ and C$_1$ are related to the charge (e-h) recombination resistance (R$_{rec}$) and dielectric relaxation capacitance of perovskite layer. The second RC element in equivalent circuit is attributed to the interfacial charge transfer resistance (R$_3$) and capacitance due to the charge accumulation at the interface of perovskite layer and SC.[25] This aid is responsible for the features appearing at high frequency in the Nyquist plot.[26–28] As discussed above the LF response is related to the ionic migration and dielectric relaxation process in perovskite layer while HF element describe the interfacial charge transfer and recombination process at perovskite and charge SC interface. To improve the fitting quality, constant phase elements (CPE) were used instead of ideal capacitors. CPEs are typically used to model the behavior of the capacitance in an inhomogeneous layer or interfaces due to roughness or variations in the thickness.[29,30] The time constant for both interfacial and bulk phenomenon were estimated from the fitting parameters of corresponding semicircles and we noted that the bulk relaxation process take place in the time scale of $10^{-4}\ s$ for all devices. On the contrary, the interfacial time varies between $10^{-1}\ s - 10^{-3}\ s$ depending on the device architects used. The device with HSC (*Spiro*-OMeTAD) showed lowest time constant while the device with ESC (c-TiO$_2$) gave highest time constant value. The high charge accumulation at HSC is due to high concentration of MA$^+$ cation as compared to I$^-$,[42] which led to higher charge accumulation at HSC

interface as compared to ESC interface (Figure 8). While, the device fabricated from $(FAPbI_3)_{0.85}(MAPbBr_3)_{0.15}$, the interfacial components reveals slightly higher degree of charge accumulation at $TiO_2/(FAPbI_3)_{0.85}(MAPbBr_3)_{0.15}$ interface as compared to $TiO_2/MAPbI_3$ interface. From the fitting parameters, we noted that the recombination resistance in $(FAPbI_3)_{0.85}(MAPbBr_3)_{0.15}$ is higher as compared to $MAPbI_3$. This is due to lower recombination current in mixed perovskite.
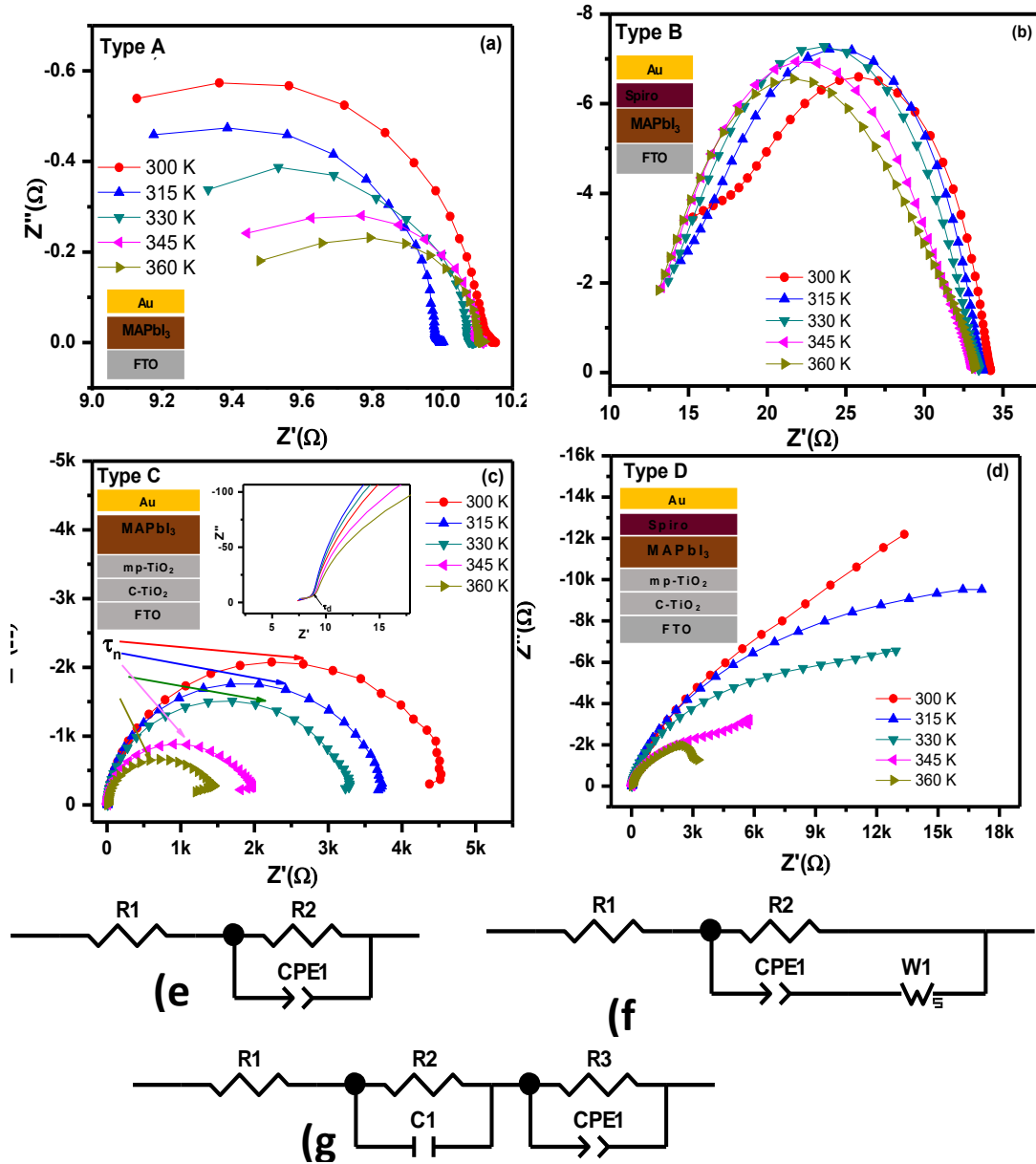

Figure 2. Impedance spectroscopy (IS) at different temperatures for (a) Type A (b),Type B (c),type C (d) type D and equivalent circuit (e) of type A & C, (f) type B and (f) type D.
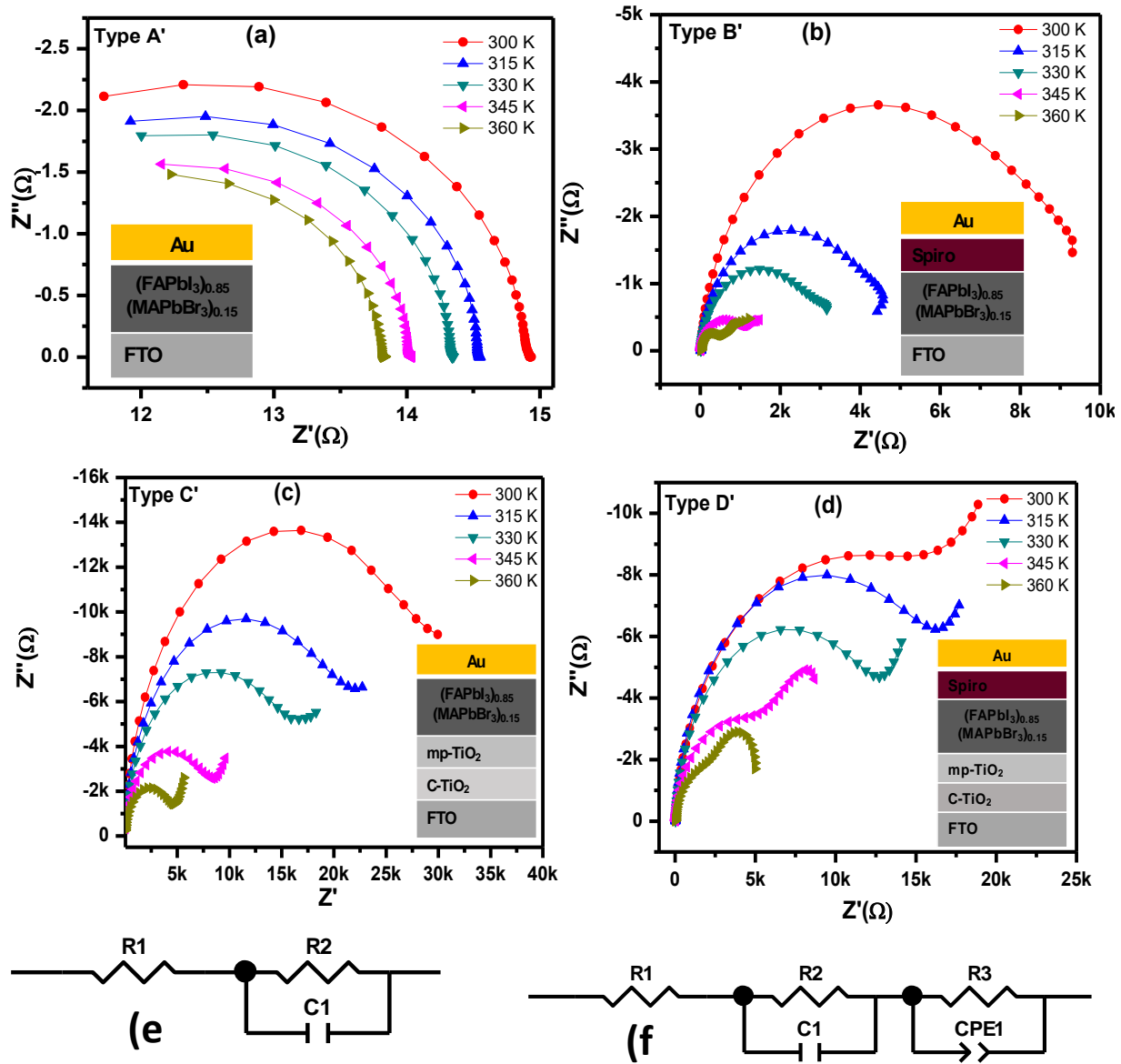
Figure 3. Impedance spectroscopy (IS) at different temperatures for (a) type A´ (b) type B´ (c) type C´ (d) type D´ and equivalent circuit (e) type A´ (f) type B´-D´.

Moreover, higher interfacial and lower dielectric relaxation capacitance in $(FAPbI_3)_{0.85}(MAPbBr_3)_{0.15}$ are attributed to its higher charge accumulation at the interface and weak dielectric relaxation. Recombination time (τ_n) deduced from peak position of IS (e.g. Figure 2c) are presented in Table 2 and Table 3. Additionally, the full devices showed higher recombination time as compared to unfinished devices. This suggest that charge SC, specifically, ESC, play a vital role in reducing the recombination current. The temperature dependence of recombination resistance R_{rec} (Figure 4) obtained from the fitting of above equivalent circuit,

7

shows that the recombination resistance of all devices decreases with temperature due to increase in carriers concentration at higher temperature. Moreover, the devices with mixed perovskite showed higher value of R_{rec} in all configuration, supports reduced recombination in (FAPbI$_3$)$_{0.85}$(MAPbBr$_3$)$_{0.15}$ as compared to MAPbI$_3$. Additionally, the highest R_{rec} value was deduced for devices with only ESC, therefore TiO$_2$ play a major role in reducing the recombination current in perovskite solar cells.
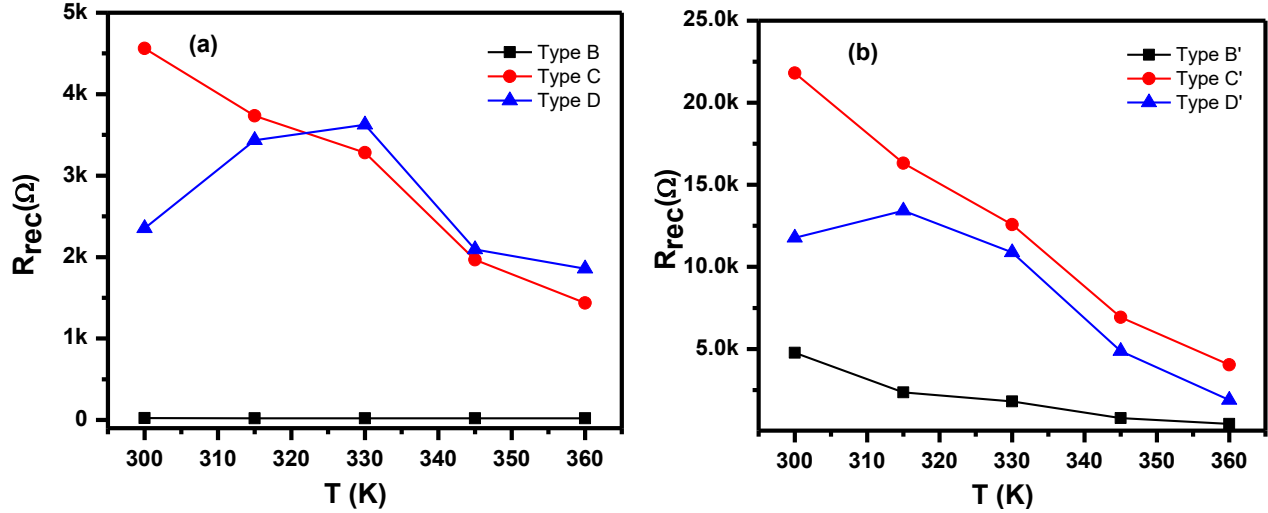

Figure 4. Recombination resistance as a function of temperature for (a) MAPbI$_3$ and (b) (FAPbI$_3$)$_{0.85}$(MAPbBr$_3$)$_{0.15}$.

By the analysis of IS we have also derived the diffusion mobility μ of charge carriers in perovskite layer through the relation: $\mu = {eD}/{k_B T}$, where k_B is the Boltzmann constant, T is absolute temperature, e is electronic charge and D is the chemical diffusion coefficient.[31–33] The electron diffusion coefficient was evaluated from the equation: $D = {L^2}/{\tau_d}$, where L is thickness of perovskite layer and τ_d is carrier transit time.[34] Transits time was calculated from IS as shown in Figure 2c. The diffusion time differ with device configuration and the type of perovskite used (Table 2 and 3). The devices with MAPbI$_3$ gave a diffusion time in the order of 10^{-5} to 10^{-7} s while devices with (FAPbI$_3$)$_{0.85}$(MAPbBr$_3$)$_{0.15}$ yielded slightly lower diffusion time in the range of 10^{-6} to 10^{-8} s. The calculated mobility are shown in Figure 5 and the devices with (FAPbI$_3$)$_{0.85}$(MAPbBr$_3$)$_{0.15}$ shows nearly two order of higher carrier mobility as compared to

MAPbI$_3$ devices. Higher mobility in (FAPbI$_3$)$_{0.85}$(MAPbBr$_3$)$_{0.15}$ is due to the reduced recombination current. The devices fabricated with hole SC (Type B & B') showed lowest mobility while highest mobility was found for the devices with ESC. The specific value of mobility are tabled in Table 2 and 3. The mobility of Type D' is lower than of Type C' due to improved carrier recombination (Figure 4b and Table 2). The devices fabricated with HSC gave lowest carrier mobility, arguably due to low carrier mobility of Spiro-OMeTAD (10^{-5} cm^2/V.s) which impedes the charge diffusion through it. Other plausible reason for low carrier mobility of devices with HSC can be imbalance cations MA$^+$ and anions I$^-$ mobility in devices.[42] Generally the diffusion coefficient of I$^-$ is about an order lower than that of MA$^+$ which allows slow cation migration and thus lower mobility.[41]
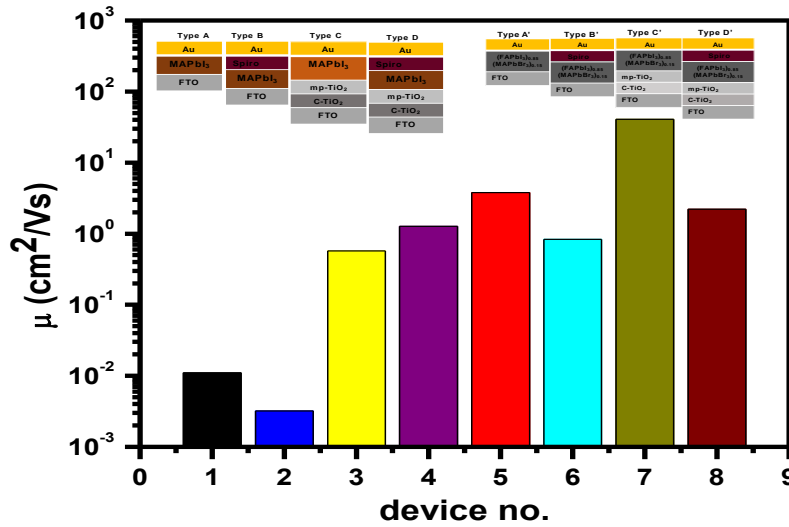

Figure 5. Charge carrier mobility in perovskite at 300 K in different device configurations.

Figure 6 displays the variation of capacitance (C) and conductance (G) as a function of frequency at different temperatures. The *C-f* graph shows three distinct regions at: low frequency (LF), intermediate frequency (IF) and high frequency (HF). In LF region (20 Hz – 1 kHz) capacitance decreases with frequency and is temperature dependent. In the IF range (1 kHz – 100 kHz) a stable plateau was noted and capacitance value was found to be independent of frequency, however it shifted to a lower value with an increase in temperature. The stable plateau in IF range corresponds to dielectric relaxation in the perovskites layer and determined by the geometrical capacitance per unit area $C_g = \varepsilon \varepsilon_0 / L$, where ε is dielectric constant of perovskite, ε_0 is the vacuum permittivity and L is the layer thickness.[35] With an increase in temperature the geometrical capacitance of selective contact free devices decreases while the devices with selective contact show constant

geometrical capacitance (Figure S8). With an increase in temperature, the geometrical capacitance of devices without selective contact (Type A & A') decreases suggesting higher degree of charge recombination in light absorbing layer (perovskite). Moreover, the ions residing at the interface acquires sufficient thermal energy to leave the interface and migrate towards the bulk (Figure 7a) and acquire lower capacitance value. The devices without selective contact (Type A & A') gave lowest capacitance as compared to other devices, pointing towards low degree of charge accumulation at interface as most of the charge carriers recombined in this case. While in the case of HF region (100 kHz – 2 MHz), capacitance decreases with frequency. The drop in capacitance at HF corresponds to the effect of the series resistance caused by electrode contact. In LF region, the capacitance drops rapidly with frequency as compared to TiO_2-free devices (type A, B & type A', B'). The drop of LF capacitance is ascribed to the polarization of interfaces owing to charge accumulation at the TiO_2/perovskite and perovskite/*Spiro-OMeTAD* interfaces.[36–39] The devices fabricated with mixed perovskite showed similar trend, suggesting low frequency behavior is related to interfacial properties rather than bulk. The devices with electron selective contact (Type C & C') reveal pronounced decrease in LF capacitance while the capacitance of devices with *Spiro*-OMeTAD (Type B, & type B') decreases slowly. Low carrier mobility of TiO_2 and energy level mismatch in TiO_2/perovskites can also led to charge accumulation at the TiO_2/perovskite interface.[40] Another plausible reason for charge accumulation at TiO_2/perovskite interface might be weak interactions between Ti−I which easily accommodate the charge carriers at the interface.[41] The devices fabricated with $(FAPbI_3)_{0.85}(MAPbBr_3)_{0.15}$ gave slightly lower capacitance pointing towards the decrease of dielectric relaxation process in these devices leading to better charge transfer and improvement in carrier mobility.
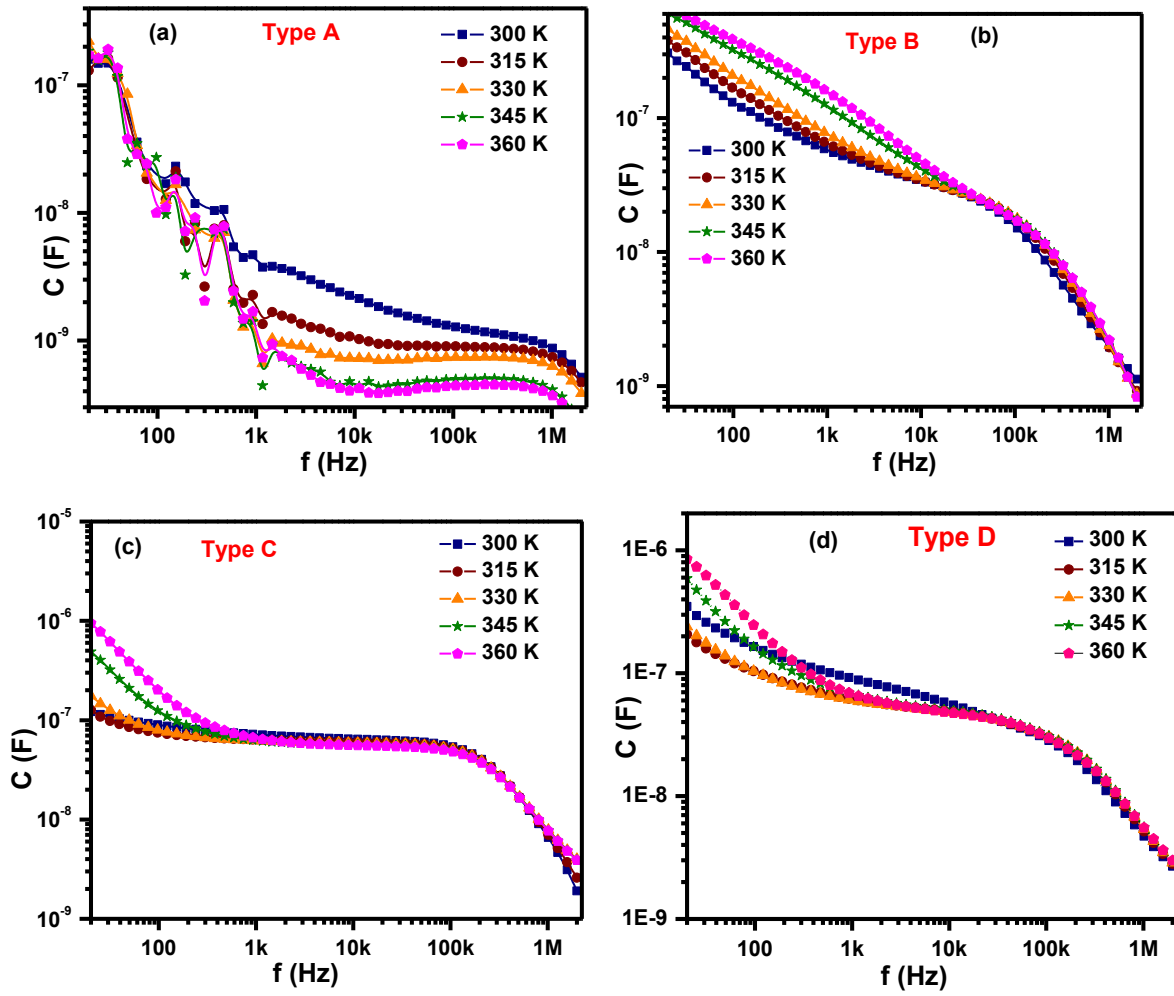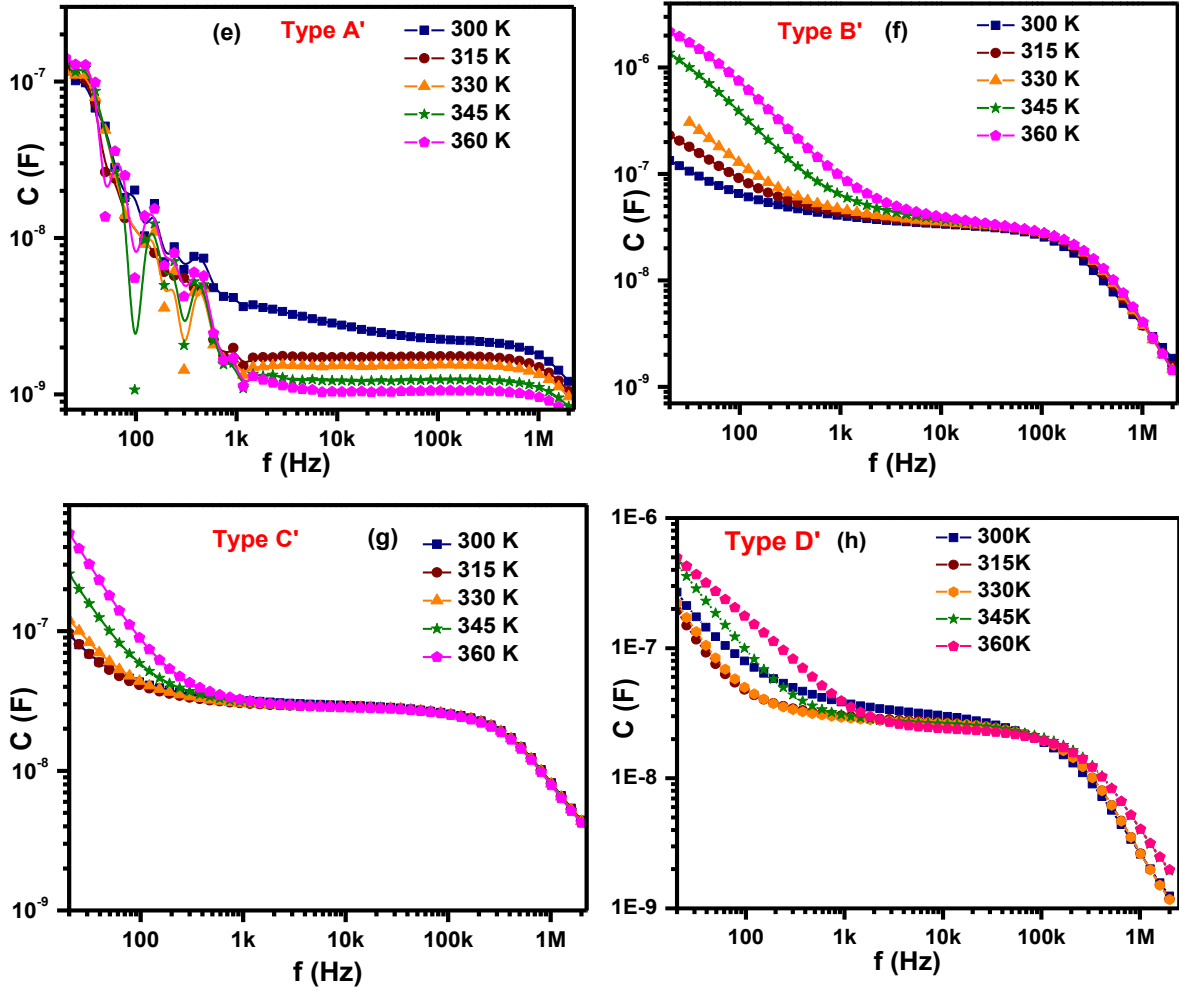
Figure 6. Capacitance as a function of frequency at different temperatures for (a) type A (b)type B (c) type C (d) type D (e) type A' (f) type B' (g) type C' (h) type D'.

Figure 7 shows the temperature dependence low frequency (~ 62 Hz) capacitance of $MAPbI_3$ and $(FAPbI_3)_{0.85}(MAPbBr_3)_{0.15}$ based devices. It can be noted (Figure 7), that the devices with HSC (type B & B') gave highest interfacial capacitance while the devices without any selective contact (type A & A') yielded lowest capacitance. These results suggest higher charge accumulation at perovskite/Spiro-OMeTAD interfaces as compared to TiO_2/perovskite interface (Figure 8). The higher charge accumulation at perovskite/Spiro-OMeTAD interface is due to (i) higher concentration of MA^+ as compared to I^- and (ii) the diffusion coefficient of MA^+ is smaller than of I^-.[42, 43] Moreover, the hole selective layer *Spiro*-OMeTAD possesses low charge mobility. Due to unbalance charge extraction and transport this will allow capacitance to build-up at perovskite/HSC. Without any selective contacts, no such electrical interface can be formed and subsequently no losses at interface. In this case the capacitance will be mainly in the bulk of

12

perovskites, while interfacial capacitance is not significant. Additionally, it can be noted (Figure 7) that the capacitance first decreases with increase in temperature until 315 K, thereafter the capacitance of devices start increasing further with temperature. Such kind of capacitance behavior indicates ferroelectric-to-paraelectric transition, which originates due to phase transition of perovskites from tetragonal to cubic structure in the temperature range 315 – 330 K.[44] It is worthy to note that devices without selective contact shows on par behavior as of devices with selective contact. These findings reveal that the low frequency response is not only limited to interface charge accumulation but also related to the ferroelectric effect or an ion movement inside perovskite layer.[45–47] Moreover, Figure S8 imply that the intermediate and high frequency signals shows less variation with temperature as of low frequency signal. Suggesting that the high frequency response are attributed to electronic process whereas the low frequency response are due to interfacial charge accumulation and ionic migration near the interface.[47]
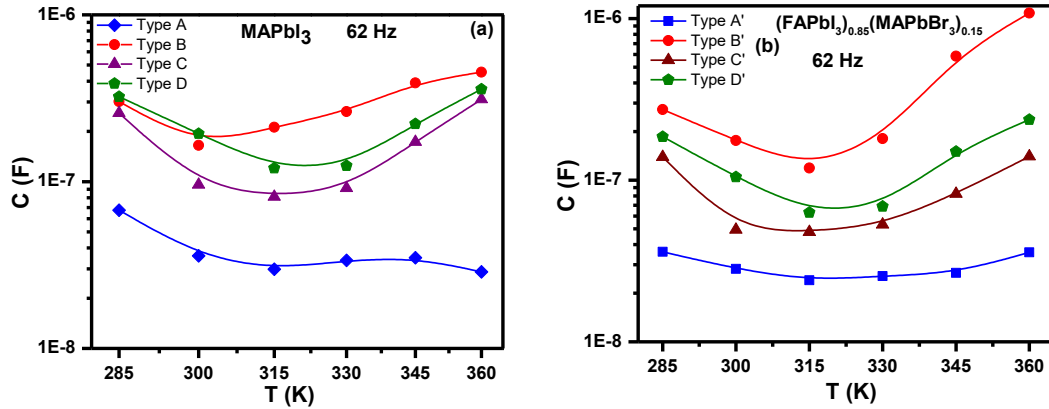
Figure 7. Temperature dependence of low frequency capacitance of a) $MAPbI_3$ and b) mixed $(FAPbI_3)_{0.85}(MAPbBr_3)_{0.15}$ perovskite based devices.

To analyze the distribution of density of state (DOS) within the bandgap of the perovskites, the emission rate of electrons from the trap states and traps activation energy[48,49] Capacitance vs. frequency (C-f) measurements at different temperatures was undertaken. In this process, with the decrease in frequency, deeper traps participate in capacitance, and thus increase in capacitance can be noted.

13
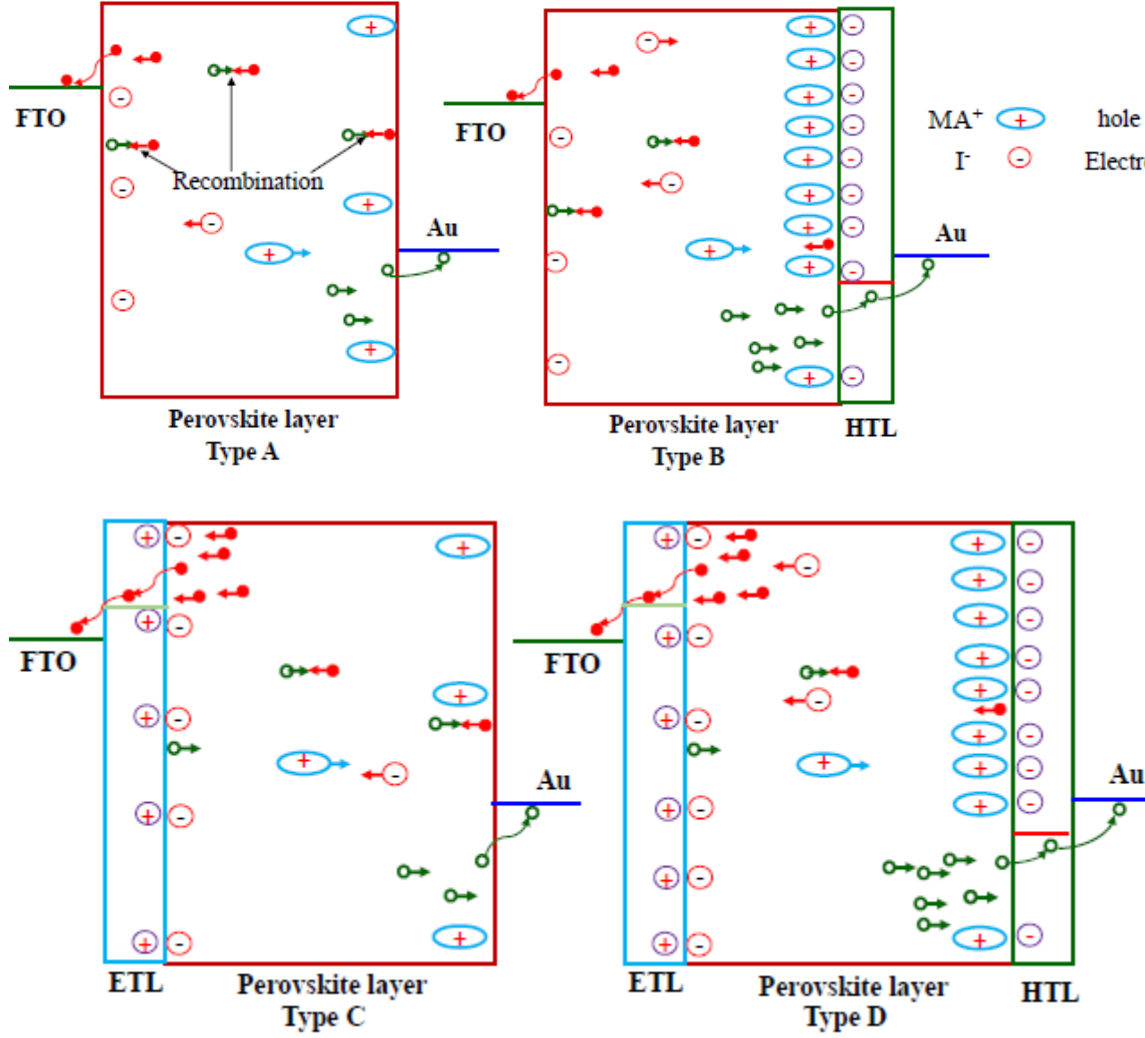
Figure 8. Schematic to depict the charge recombination and accumulation at ETL/perovskite and perovskite/HTL interface.

The emission rate of a charge carrier from a trap state at a given frequency strongly depends upon the energy of the trap and the temperature of device. The emission rate of electrons from a trap state located below E_T to the conduction band edge E_C is given by the relation:[50–52]

$$e_n = N_C v_{th} \sigma_n \exp\left(-\frac{E_C - E_T}{k_B T}\right) \tag{1}$$

where N_C is the effective density of states in the conduction band, v_{th} is the root mean square thermal velocity of electrons, σ_n is the capture cross section of trap and the product $N_C v_{th} \sigma_n$ is

called the attempt to escape frequency (ATEF) denoted by υ_0. Since $N_C \propto T^{3/2}$ and rms speed $v_{th} \propto T^{1/2}$, consequently, ATEF $\upsilon_0 \propto T^2$, then equation 1 can be transformed to

$$\ln\left(\frac{e_n}{T^2}\right) = \ln\xi - \frac{E_A}{k_B T} \tag{2}$$

where ξ is the proportionality constant and $E_A = E_C - E_T$ is the activation energy of the traps. From the slope of Arrhenius plot, $\ln\left(\frac{f_{peak}}{T^2}\right) vs.\frac{1}{T}$ (Figure S9) the value of activation energy can be deduced and the intercept of the line provide the value of ATEF. Where f_{peak} is peak frequency extracted from [-f dC/df] vs. frequency plot shown in Figure 9. The calculated activation energy for devices are presented in Table 2 and 3. The activation energy is ~55.57 meV for charge selective contact free devices that slightly decreases for the devices with selective contact. The ATEF is 1.81×10^9 Hz for selective contact free devices and increase to 3.55×10^9 Hz (MAPbI$_3$) and 2.35×10^9 Hz (Mixed perovskite) for the devices with SC and are in the customary range for organo-lead perovskites[49].
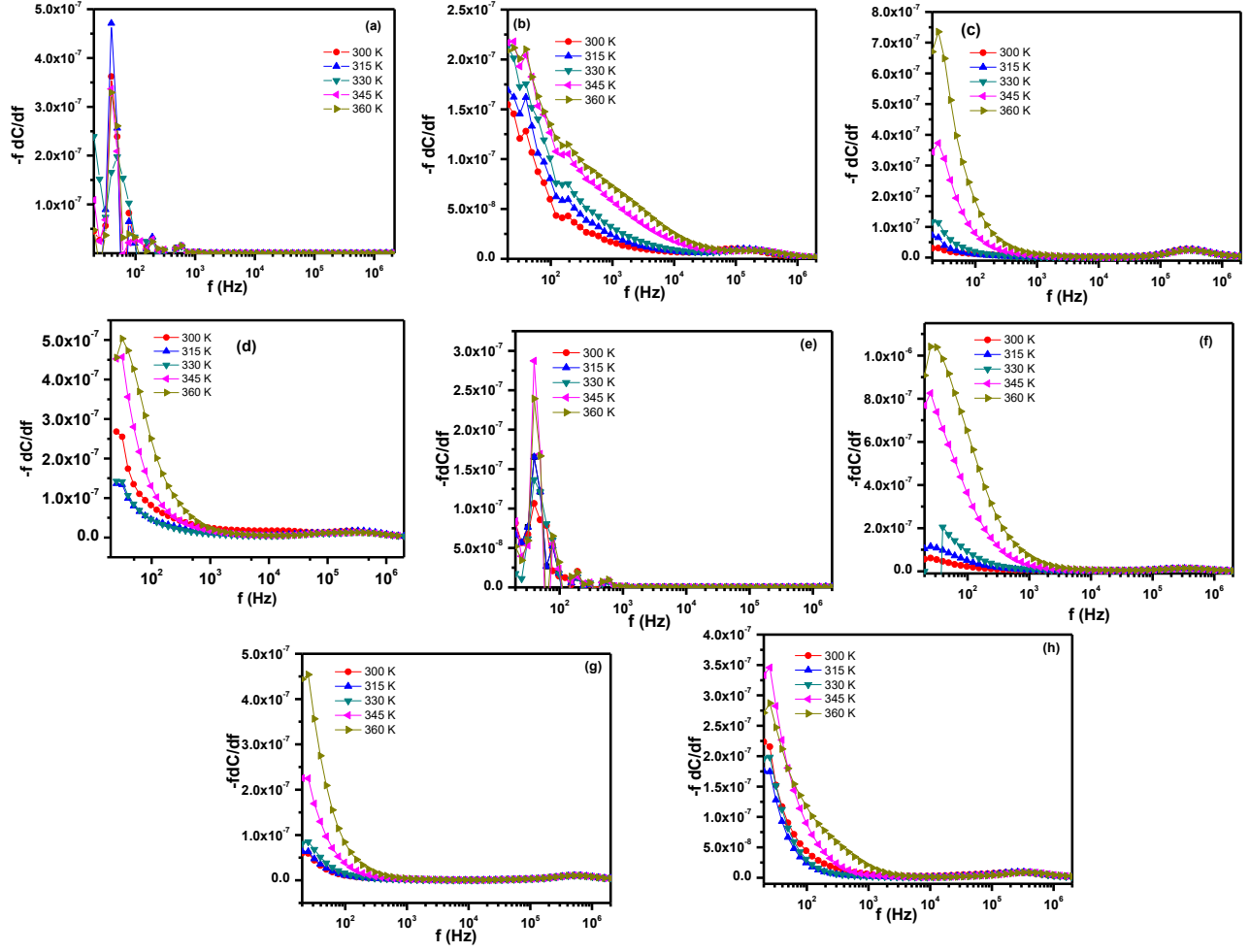
Figure 9. f × dC/df vs. frequency at different temperatures for (a) Type A, (b) Type B, (c) Type C, (d) Type D, (e) Type A', (f) Type B', (g) Type C', (h) Type D'.

Figure 9 show the experimental data for [-f dC/df] vs. frequency, measured at various temperatures for MAPbI$_3$ and (FAPbI$_3$)$_{0.85}$(MAPbBr$_3$)$_{0.15}$. There is a secondary peak related to a deeper trap in addition to the shallow traps near the edge of conduction band. The density of states (N_C) at the edge of conduction band (shallow traps) deduced from these plots is ~2.70×10^{14} cm^{-3} for selective contact free devices and the value increases for devices with selective contact. The device fabricated from MAPbI$_3$ have slightly higher density of state of N$_C$ ~4.62×10^{14} cm^{-3} as compared to the (FAPbI$_3$)$_{0.85}$(MAPbBr$_3$)$_{0.15}$ of ~1.82×10^{14} cm^{-3}.

The density distribution of trap states was evaluated by using Mott−Schottky analysis and admittance spectroscopy. The distribution of trap state density can be derived from the equation:[58]

$$N_T = -\frac{V_{bi}}{qWk_BT}\left(f\frac{dC}{df}\right) \tag{3}$$

$$E_\omega = k_BT\ln\left(\frac{\omega_0}{\omega}\right) \tag{4}$$

where V_{bi} is the built-in potential, W is the depletion width, q is the elementary charge, and ω is the applied angular frequency. A Mott-Schottky plot: $\frac{1}{C^2} = \frac{2(V_{bi}-V)}{Aq\varepsilon\varepsilon_0 N}$ of device D and D'

measured at 10 kHz is shown in Figure 10 (a). The slope of straight line gives the impurity doping density N and intersection on the voltage axis determines V_{bi}. The depletion width corresponds to the zero bias was calculated by equation:

$$W = \sqrt{\frac{\varepsilon\varepsilon_0 V_{bi}}{qN}} \tag{5}$$

and found to be 206 nm and 261 nm for device D and D', respectively. The built in potential for device type D and D' was found to be 0.69 V and 1.05 V respectively. From these results, the density distribution and energy levels of trap states at 300 K in these devices are displayed in Fig. 10b. It can be observed from Figure that the peak value of traps in device D and D' are located at 0.42 eV and 0.70 eV with peak value of 1.37×10^{17} (eV cm^3)$^{-1}$ and 8.84×10^{16} (eV cm^3)$^{-1}$, respectively.
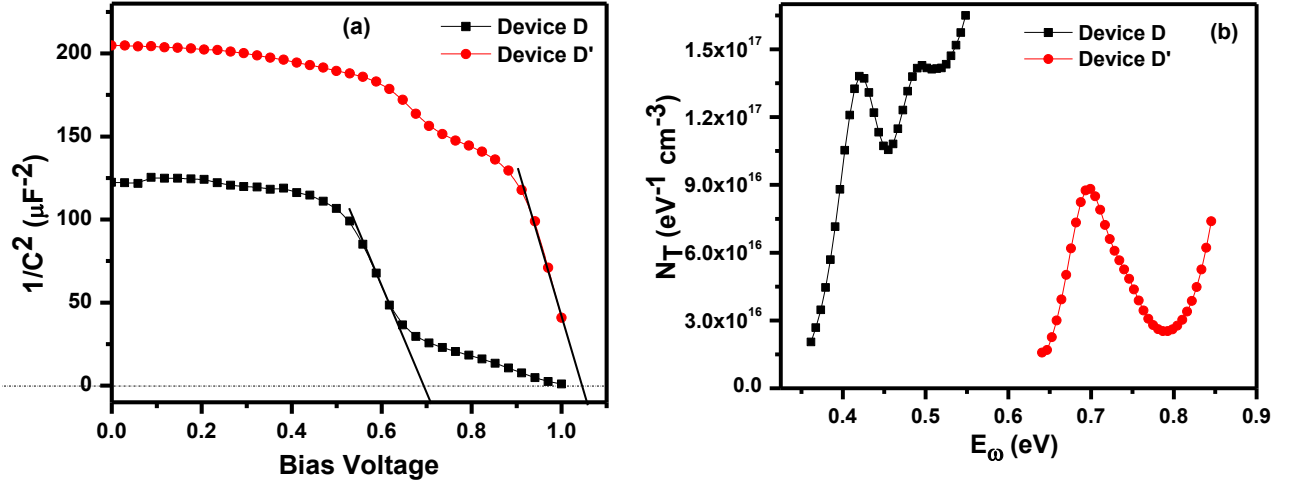
Figure 10. (a) Mott−Schottky analysis of device D and D' at 10 kHz, **(b)** trap state density (N_T) of device D and D' measured at 300 K.

Table 2. Electrical parameters calculated for MAPbI$_3$ perovskite at 300 K.

Parameters/devices	Type A	Type B	Type C	Type D
μ (cm^2/V.s)	1.1×10^{-2}	3.19×10^{-3}	5.7×10^{-1}	1.27
Diffusion time τ_d (μs)	14.3	55.45	1.57	0.308
Recombination time τ_n (μs)	0.100	1.88	338	6366
Activation energy E_A (meV)	55.57	55.57	55.57	82.96
ATEF ν_0 (Hz)	1.77×10^9	3.48×10^9	3.48×10^9	5.40×10^{12}

Table 3. Electrical parameters calculated for mixed perovskite at 300 K.

Parameters/devices	Type A'	Type B'	Type C'	Type D'
μ (cm^2/V.s)	3.78	0.83	40.55	2.21
Diffusion time τ_d (ns)	540	2460	196	386
Recombination time τ_n (μs)	0.100	423	1320	1300
Activation energy E_A (meV)	55.57	50.54	50.54	124
ATEF ν_0 (Hz)	1.77×10^9	2.30×10^9	2.30×10^9	2.13×10^{17}

Conclusions

Herein, we have investigated the role of electron and hole selective contact (SC) in perovskite solar cells by means of impedance spectroscopy. The devices fabricated with (FAPbI$_3$)$_{0.85}$(MAPbBr$_3$)$_{0.15}$ shows higher charge accumulation at perovskite/SC interface as compared to MAPbI$_3$ based one. Moreover, we have also noted that charge accumulation at hole selective interface is higher as compared to electron selective interface. The devices fabricated with both (electron and hole) SC

18

shows low level of recombination as compare to the devices without any SC that shows high degree of recombination. $(FAPbI_3)_{0.85}(MAPbBr_3)_{0.15}$ based devices gave reduced recombination and high carrier mobility. The maximum mobility for $MAPbI_3$ and $(FAPbI_3)_{0.85}(MAPbBr_3)_{0.15}$ was found to be 1.27 and 40.55 cm^2/Vs at room temperature (300 K), respectively in our experimental setup. In order to elucidate the DOS and trap states in the band gap of perovskites, temperature dependent C-f experiments were used. The activation energy for both perovskite was found to be 55.57 meV for SC-free devices, however this parameter increases and represent a value of 123 meV (for mixed perovskite) and 82.96 meV (for $MAPbI_3$) for devices fabricated with both electron and hole SC. The peak value of traps in $MAPbI_3$ and mixed perovskite devices are located at 0.42 eV and 0.70 eV with peak value of 1.37×10^{17} and 8.84×10^{16} eV^{-1} cm^{-3}, respectively.

Experimental part

Device fabrication details

FTO-coated glass (TEC15, Pilkington) patterned by laser etching was employed for the fabrication of perovskite based solar cells. Substrates were cleaned by ultrasonication in three different solutions with the aim to eliminate any possible contamination. First a Hellmanex® solution (2%) were used and rinsed with deionized water and ethanol. Then samples were ultrasonicated for 30 minutes in acetone, and 2-propanol and finally they were dried by using nitrogen. After this step, a TiO_2 compact layer was deposited by spray pyrolysis at 450 ºC using titanium (IV) diisopropoxide bis(acetyl acetonate) precursor solution (1/19 v/v ratio in ethanol, Sigma Aldrich) using oxygen as a carrier gas. The TiO_2 blocking layer was then kept for 30 minutes at 450 ºC for the formation of anatase phase. After the samples attained room temperature, the ESC i.e TiO_2 mesoporous layer (Dyesol, 30NRD) was deposited by spin coating (4,000 rpm for 20 s) and annealed at 500 ºC using ramp heating process. Subsequently, pure methyl ammonium ($MAPbI_3$) or mixed cation perovskite (($FAPbI_3)_{0.85}(MAPbBr_3)_{0.15}$) was then deposited according to our previous reports[12,39]. All solutions were prepared inside an argon glove box under controlled moisture and oxygen conditions (H_2O level: <1 ppm and O_2 level: <10 ppm). Optimized concentrations were prepared depending on the perovskite fabricate (1.2M and 1.4M) respectively. The perovskite solution was spin coated in a two steps setup at 1000 and 5000 rpm for 10 and 20s respectively. During the second step, 110μL of chlorobenzene was dropped on the spinning substrate 15 seconds before the end of the spinning program as an anti-solvent approach. The

samples were then annealed (100°C) for 1h in an argon filled glove box. After perovskite deposition, annealing and cool down, 35 μL of a Spiro-OMeTAD solution was then spin coated at 4000 rpm for 20 seconds as hole transporting material. Spiro-OMeTAD material (70mM) were dissolved in 1 mL of chlorobenzene using standard additives as 17.5 μL of a lithium bis(trifluoromethylsulphonyl)imide (LiTFSI) stock solution (520 mg of LiTFSI in 1mL of acetonitrile), 21.9 μL of a FK209 (Tris(2-(1H-pyrazol-1-yl)-4-tertbutylpyridine) cobalt(III)Tris(bis(trifluoromethylsulfonyl)imide))) stock solution (400 mg in 1 mL of acetonitrile) and 28.8 μL of 4-tert-butylpyridine (*t*-BP). For all devices, 80 nm of gold was deposited by thermal evaporation under a vacuum level between 1×10^{-6} and 1×10^{-5} torr.

Device characterization

Cross-sectional and top-view microstructure were recorded by a Hitachi S-4800 scanning electron microscope and used for thickness evaluation. Impedance measurements at different temperatures were performed on a Keysight precision LCR meter model No. E4980A. Samples were measured at different temperatures (300 – 360 K) using a Linkam sample chamber heating stage filled with nitrogen in a closed environment, to control the degradation of the samples for humidity conditions. After measurement, data were fitted by Z-view (version 3.1c) software in order to extract characteristic parameters of the cells.

Conflicts of interest

The authors declare no conflict of interest.

References

1   N. J. Jeon, J. H. Noh, W. S. Yang, Y. C. Kim, S. Ryu, J. Seo, S. Il Seok, *Nature* **2015***, 517,* 470-480.

2   M. Saliba, T. Matsui, J. Y. Seo, K. Domanski, J. P. Correa-Baena, M. K. Nazeeruddin, S. M. Zakeeruddin, W. Tress, A. Abate, A. Hagfeldt, M. Grätzel, *Energy Environ. Sci.* **2016**,

9, 1989-1997; S. Kazim, M.^^K. Nazeeruddin, M. Grätzel, S. Ahmad, *Angew. Chem. Int. Ed.* **2014**, *53*, 2812--2824; *Angew. Chem.* **2014**, *126*, 2854--2867</jnl>.

3   NREL Efficiency Chart. http://www.nrel.gov/ncpv/images/ efficiency_chart.jpg.

4   Q. Zhang, R. Su, W. Du, X. Liu, L. Zhao, S. T. Ha, Q. Xiong, *Small Methods* 2017, **1**, 1700163.

5   T. Matsushima, C. Qin, K. Goushi, F. Bencheikh, T. Komino, M. Leyden, A. S. D. Sandanayaka, C. Adachi, *Adv. Mater.* **2018**, 1802662 , DOI:10.1002/adma.201802662.

6   Z. Xiao, R. A. Kerner, L. Zhao, N. L. Tran, K. M. Lee, T. W. Koh, G. D. Scholes, B. P. Rand, *Nat. Photonics* **2017**, *11,* 108–115.

7   B. Chen, M. Yang, X. Zheng, C. Wu, W. Li, Y. Yan, J. Bisquert, G. Garcia-Belmonte, K. Zhu, S. Priya, *J. Phys. Chem. Lett.* **2015**, *6,* 4693–4700.

8   S. Van Reenen, M. Kemerink, H. J. Snaith, *J. Phys. Chem. Lett.* **2015**, *6,* 3808-3814.

9   H. Yu, H. Lu, F. Xie, S. Zhou and N. Zhao, *Adv. Funct. Mater.* **2016**, *26,* 1411-1419.

10   Y. Shao, Z. Xiao, C. Bi, Y. Yuan and J. Huang, *Nat. Commun.* **2014**, *5*:5784, DOI:10.1038/ncomms6784.

11   L. K. Ono, Y. Qi, S. (Frank) Liu, *Joule* **2018**, *2*, 1961-1990.

12   M. Salado, J. Idigoras, L. Calio, S. Kazim, M. K. Nazeeruddin, J. A. Anta, S. Ahmad, *ACS Appl. Mater. Interfaces* **2016**, *50,* 34414–34421.

13   Y. Yuan, J. Huang, *Acc. Chem. Res.* **2016**, *49*, 286–293.

14   Z. Li, C. Xiao, Y. Yang, S. P. Harvey, D. H. Kim, J. A. Christians, M. Yang, P. Schulz, S. U. Nanayakkara, C. S. Jiang, J. M. Luther, J. J. Berry, M. C. Beard, M. M. Al-Jassim and K. Zhu, *Energy Environ. Sci.* **2017**, *10*, 1234–1242.

15   S. Cacovich, L. Ciná, F. Matteocci, G. Divitini, P. A. Midgley, A. Di Carlo and C. Ducati, *Nanoscale* **2017**, *9*, 4700–4706.

16   L. Caliò, M. Salado, S. Kazim, S. Ahmad, *Joule* **2018**, *2,* 1800–1815.

17   E. J. Juarez-Perez, R. S. Sanchez, L. Badia, G. Garcia-Belmonte, Y. S. Kang, I. M. Sero, J. Bisquert, *J. Phys. Chem. Lett.* **2014**, *5*, 2390-2394.

18   H. Tsai, R. Asadpour, J.-C. Blancon, C. C. Stoumpos, O. Durand, J. W. Strzalka, B. Chen, R. Verduzco, P. M. Ajayan, S. Tretiak, J. Even, M. A. Alam, M. G. Kanatzidis, W. Nie, A. D. Mohite, *Science* **2018**, *360,* 67-70.

19   J. M. Frost, K. T. Butler, F. Brivio, C. H. Hendon, M. van Schilfgaarde, A. Walsh, *Nano*

Lett. **2014**, *14*, 2584–90.

20   H. S. Duan, H. Zhou, Q. Chen, P. Sun, S. Luo, T. Bin Song, B. Bob, Y. Yang, *Phys. Chem. Chem. Phys.* **2015**, *17*, 112–116.

21   M. N. F. Hoque, M. Yang, Z. Li, N. Islam, X. Pan, K. Zhu, Z. Fan, *ACS Energy Lett.* **2016**, *1*, 142–149.

22   K. Wang, Y. Shi, Q. Dong, Y. Li, S. Wang, X. Yu, M. Wu, T. Ma, *J. Phys. Chem. Lett.* **2015**, *6*, 755–759.

23   J. F. Wang, L. Zhu, B. G. Zhao, Y. L. Zhao, J. Song, X. Q. Gu, Y. H. Qiang, *Sci. Rep.* **2017**, *7*, 14478.

24   A. Todinova, L. Contreras-Bernal, M. Salado, S. Ahmad, N. Morillo, J. Idígoras, J. A. Anta, *ChemElectroChem* **2017**, *4*, 2891–2901.

25   E. J. Juarez-Perez, M. Wußler, F. Fabregat-Santiago, K. Lakus-Wollny, E. Mankel, T. Mayer, W. Jaegermann, I. Mora-Sero, *J. Phys. Chem. Lett.* **2014**, *5*, 680–685.

26   V. Gonzalez-Pedro, E. J. Juarez-Perez, W. S. Arsyad, E. M. Barea, F. Fabregat-Santiago, I. Mora-Sero, J. Bisquert, *Nano Lett.* **2014**, *14*, 888–893.

27   A. Dualeh, T. Moehl, N. Tétreault, J. Teuscher, P. Gao, M. K. Nazeeruddin, M. Grätzel, *ACS Nano*, **2014**, *8*, 362–373.

28   H. S. Kim, I. Mora-Sero, V. Gonzalez-Pedro, F. Fabregat-Santiago, E. J. Juarez-Perez, N. G. Park, J. Bisquert, *Nat. Commun.* **2013**, *4*, 2242.

29   W. H. Mulder, J. H. Sluyters, T. Pajkossy, L. Nyikos, *J. Electroanal. Chem.* **1990**, *285*, 103–115.

30   J. Vogelsang, W. Strunz, *Electrochim. Acta* **2001**, *46*, 3619–3625.

31   G. Garcia-Belmonte, J. Bisquert, G. S. Popkirov, *Appl. Phys. Lett.* **2003**, *83,* 2178–2180.

32   G. Garcia-Belmonte, A. Munar, E. M. Barea, J. Bisquert, I. Ugarte, R. Pacios, *Org. Electron. physics, Mater. Appl.* **2008**, *9*, 847–851.

33   J. Bisquert, *Phys. Chem. Chem. Phys.* **2008**, *10*, 3175–3194.

34   J. Bisquert, *J. Phys. Chem. B* **2002**, *106*, 325–333.

35   O. Almora, C. Aranda, G. Garcia-Belmonte, *J. Phys. Chem. C* **2018**, *122*, 13450–13454.

36   O. Almora, A. Guerrero, G. Garcia-Belmonte, *Appl. Phys. Lett.* **2016**, *108*, 043903.

37   S. Ravishankar, S. Gharibzadeh, C. Roldán-Carmona, G. Grancini, Y. Lee, M. Ralaiarisoa, A. M. Asiri, N. Koch, J. Bisquert, M. K. Nazeeruddin, *Joule* **2018**, *2*, 788–798.

38   G. Garcia-Belmonte, J. Bisquert, *ACS Energy Lett.* **2016**, *1*, 683–688.

39   M. Salado, L. Calió, L. Contreras-Bernal, J. Idígoras, J. A. Anta, S. Ahmad, S. Kazim, *Materials*, **2018**, *7*, 1073.

40   I. Zarazua, J. Bisquert, G. Garcia-Belmonte, *J. Phys. Chem. Lett.* **2016,** *7*, 525–528.

41   V. Roiati, E. Mosconi, A. Listorti, S. Colella, G. Gigli, F. De Angelis, *Nano Lett.* **2014**, *14*, 2168–2174.

42   M. H. Futscher, J. M. Lee, L. McGovern, L. A. Muscarella, T. Wang, M. Irfan Haider, A. Fakharuddin, L. S.-Mende, B. Ehrler, *Mater. Horiz.* **2019**, DOI: 10.1039/c9mh00445a.

43   J. M. Azpiroz, E. Mosconi, J. Bisquert, F. De Angelis, *Energy Environ. Sci.* **2015**, *8*, 2118-2127.

44   Y. Rakita, O. Bar-Elli, E. Meirzadeh, H. Kaslasi, Y. Peleg, G. Hodes, I. Lubomirsky, D. Oron, D. Ehre, D. Cahen, *Proc. Natl. Acad. Sci.* **2017**, *114,* E5504–E5512.

45   L. Contreras, S. Ramos-Terrón, A. Riquelme, P. P. Boix, J. A. Idígoras, I. Mora Seró, J. A. Anta, *J. Mater. Chem.* **2019**, *7*, 12191-12200.

46   H. Zhang, X. Qiao, Y. Shen, T. Moehl, S. M. Zakeeruddin, M. Grätzel, M. Wang, *J. Mater. Chem. A* **2015**, *3*, 11762–11767.

47   Z. Xiao, Y. Yuan, Y. Shao, Q. Wang, Q. Dong, C. Bi, P. Sharma, A. Gruverman, J. Huang, *Nat. Mater.* **2015**, *14*, 193–197.

48   T. Walter, R. Herberholz, C. Müller, H. W. Schock, *J. Appl. Phys.* **1996**, *80*, 4411–4420.

49   M. Samiee, S. Konduri, B. Ganapathy, R. Kottokkaran, H. A. Abbas, A. Kitahara, P. Joshi, L. Zhang, M. Noack, V. Dalal, *Appl. Phys. Lett.* **2014**, *105*, 153502.

50   D. K. Schroder, *Semiconductor Material and Device Characterization: Third Edition*, **2005**.

51   R. F. Pierret, G. W. Neudeck, *Summary for Policymakers*, **1987**.

52   J. A. Carr, M. Elshobaki, S. Chaudhary, *Appl. Phys. Lett.* **2015**, *107*, 203302.

53**.**   X. Dong, D. Chen, J. Zhou, Y.Z. Zheng, X. Tao, *Nanoscale* **2018**, *10*, 7218–7227.

54.   J. Zhang, P. Barboux, T. Pauporté, *Adv. Energy Mater* **2014**, *4***,** 1400932.

55.   J. Zhang, E. José Juárez-Pérez, I. Mora-Seró, B. Viana, T. Pauporté, *J. Mater. Chem. A* **2015**, *3*, 4909-4915.

56.   J. Zhang, T. Pauporté, *J. Phys. Chem. C* **2015**, *119*, 14919–14928.

57.   H.-Seon Kim, J.-Wook Lee, N. Yantara, P. P. Boix, S. A. Kulkarni, S. Mhaisalkar, M. Grätzel, N.-Gyu Park, *Nano Lett*. **2013**, *13*, 2412−2417.

58.   N. Li et al., *Nat. Energy*, **2019**, *4*, 408-415.

SUPPORTING INFORMATION

Elucidating the impact of charge selective contact in halide perovskite through impedance spectroscopy

Mohd Taukeer Khan [a,c], *Manuel Salado* [a]*, Abdullah Almohammedi* [c] *Samrana Kazim,*[a,b] *and Shahzada Ahmad,*[a,b]*

[a] BCMaterials-Basque Center for Materials, Applications and Nanostructures, Martina Casiano, UPV/EHU Science Park, Barrio Sarriena s/n, Leioa 48940, Spain.

[b] IKERBASQUE, Basque Foundation for Science, Bilbao, 48013, Spain.

[c] Department of Physics, Faculty of Science, Islamic University of Madinah, Prince Naifbin Abdulaziz, Al Jamiah, Madinah 42351, Kingdom of Saudi Arabia.

Tel: +34 946128811 Email: shahzada.ahmad@bcmaterials.net

S1. Fitting of Impedance spectra

The fitting of impedance spectra and equivalent circuit are shown in following figures. In these figures the resistance R_1, R_2 and R_3 represents the contact resistance of wire and FTO, recombination resistance in perovskite layer and selective contacts resistance, respectively. The capacitance corresponds to R_2 represents the dielectric relaxation in perovskite and other one represents the interfacial capacitances between the perovskite and charge selective contacts (ESC and HSC).

Element	Freedom	Value	Error	Error %
R1	Free(+)	11.46	0.16058	1.4012
R2	Free(+)	22.68	0.15843	0.69854
CPE1-T	Free(+)	4.7482E-07	2.2503E-08	4.7393
CPE1-P	Free(+)	0.84468	0.0031308	0.37065
W1-R	Free(+)	7.943	0.40316	5.0757
W1-T	Free(+)	3.491E-07	9.9859E-09	2.8605
W1-P	Free(+)	0.46679	0.0099446	2.1304

Figure S1. Fitting of impedance spectra of Type B in (a) complex plane and (b and c) Bode plot

Element	Freedom	Value	Error	Error %
R1	Free(+)	7.796	0.070141	0.8997
R2	Free(+)	4561	29.405	0.64471
CPE1-T	Free(+)	1.0423E-07	2.0512E-09	1.968
CPE1-P	Free(+)	0.9589	0.0016835	0.17557
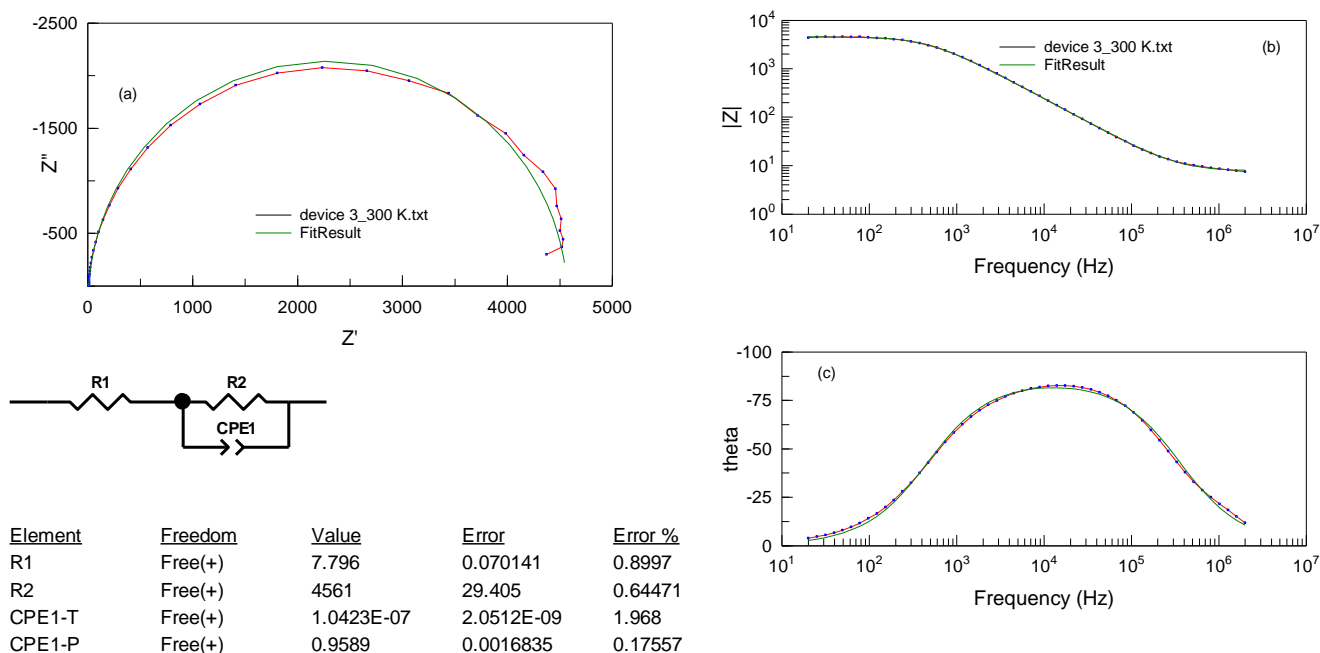
Figure S2. Fitting of impedance spectra of Type C in (a) complex plane and (b and c) Bode plot

Element	Freedom	Value	Error	Error %
R1	Free(+)	10.91	0.28613	2.6226
R2	Free(+)	2353	319.7	13.587
C1	Free(+)	2.9907E-07	2.5377E-08	8.4853
R3	Free(+)	42909	4020	9.3687
CPE1-T	Free(+)	1.2362E-06	9.651E-08	7.807
CPE1-P	Free(+)	0.74159	0.0055495	0.74832
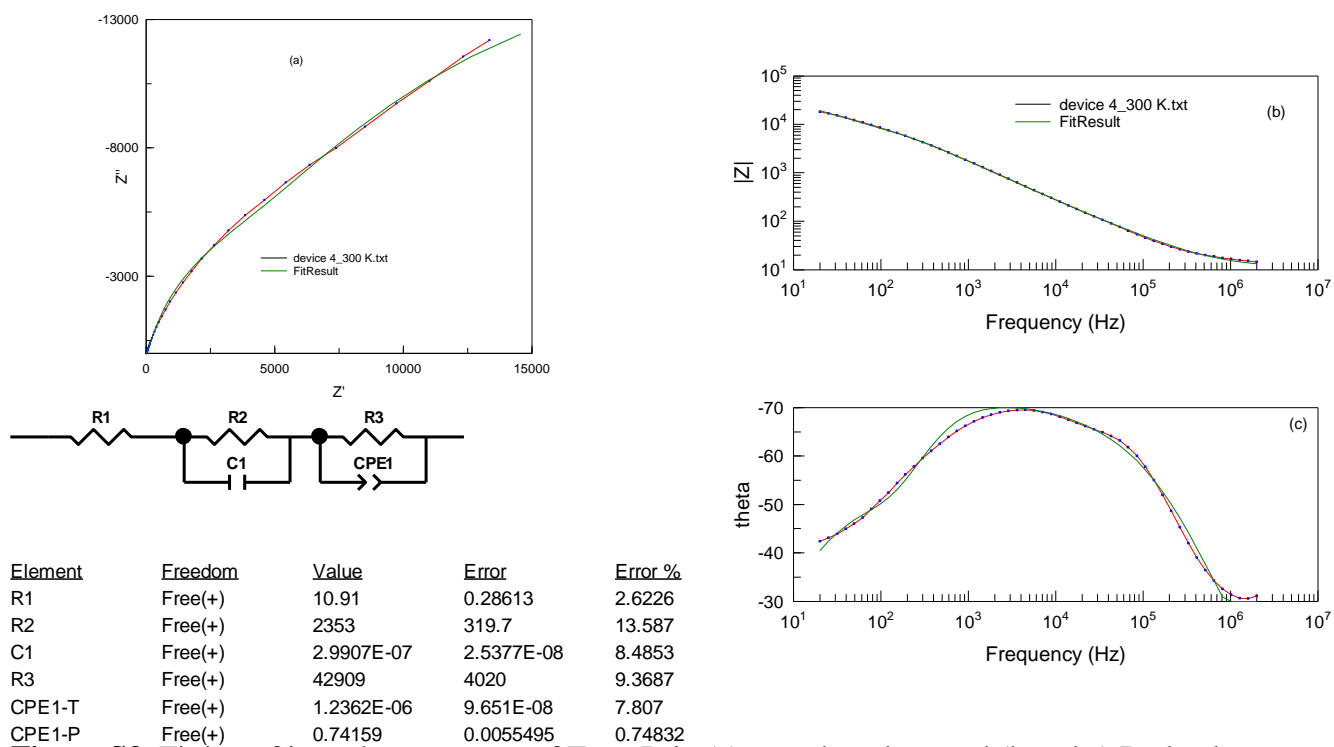
Figure S3. Fitting of impedance spectra of Type D in (a) complex plane and (b and c) Bode plot

27

Element	Freedom	Value	Error	Error %
R1	Free(+)	10.45	0.042439	0.40611
R2	Free(+)	4.451	0.043399	0.97504
CPE1-T	Free(+)	2.5566E-08	1.9444E-09	7.6054
CPE1-P	Free(+)	0.99968	0.0058422	0.58441
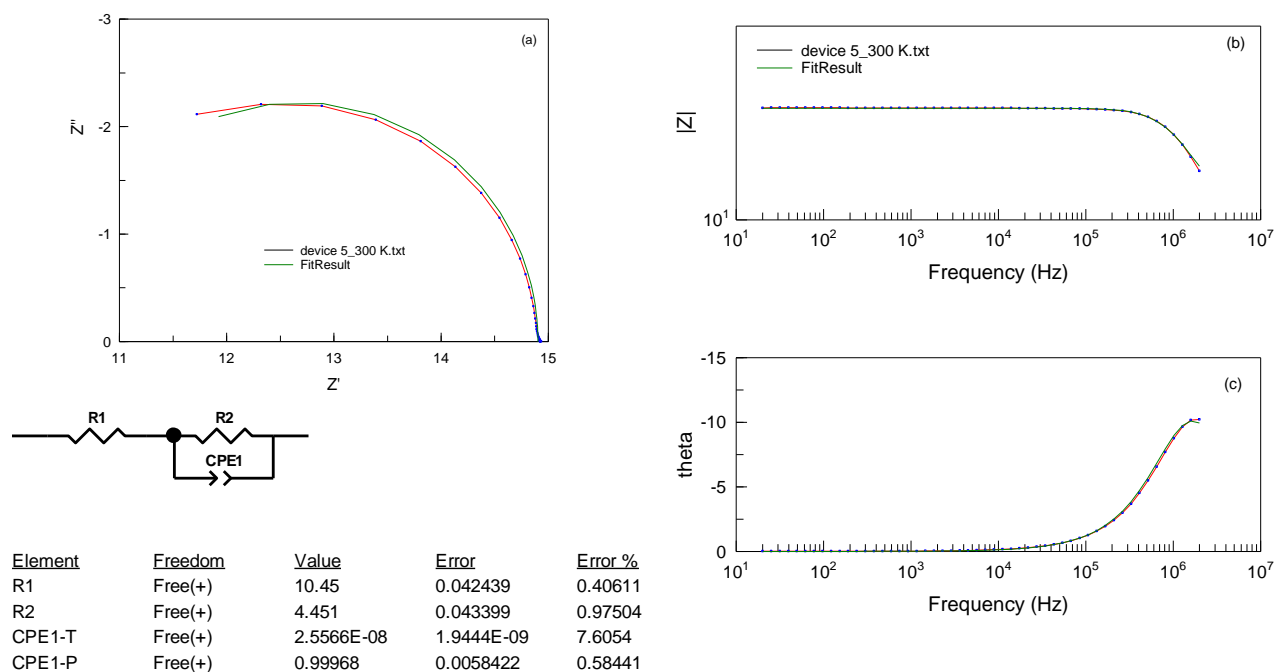
Figure S4. Fitting of impedance spectra of Type A' in (a) complex plane and (b and c) Bode plot

Element	Freedom	Value	Error	Error %
R1	Free(+)	14.99	0.28121	1.876
R2	Free(+)	4770	295.8	6.2013
C1	Free(+)	5.3709E-08	2.1632E-09	4.0276
R3	Free(+)	5649	256.3	4.5371
CPE1-T	Free(+)	1.0875E-06	2.4796E-07	22.801
CPE1-P	Free(+)	0.78456	0.01444	1.8405
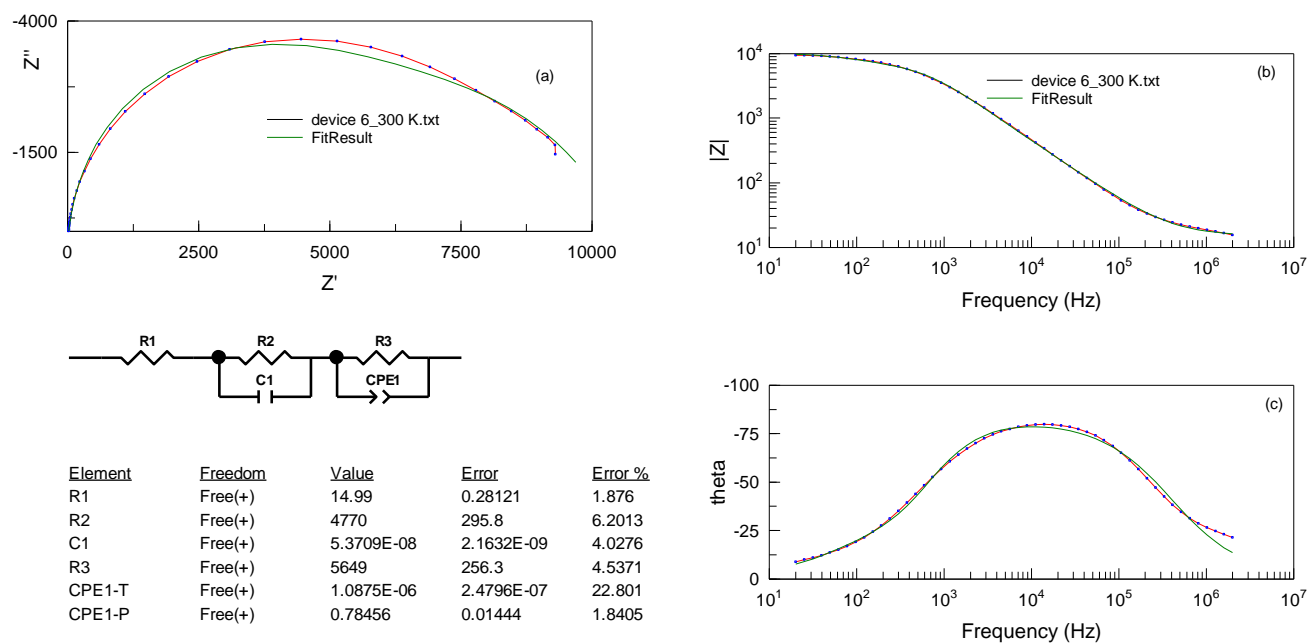
Figure S5. Fitting of impedance spectra of Type B' in (a) complex plane and (b and c) Bode plot

Element	Freedom	Value	Error	Error %
R1	Free(+)	19.54	0.28341	1.4504
R2	Free(+)	13417	243.42	1.8143
C1	Free(+)	3.447E-08	3.8178E-10	1.1076
R3	Free(+)	35463	9083.1	25.613
CPE1-T	Free(+)	3.301E-06	3.6434E-07	11.037
CPE1-P	Free(+)	0.70324	0.0079718	1.1336

Figure S6. Fitting of impedance spectra of Type C' in (a) complex plane and (b and c) Bode plot

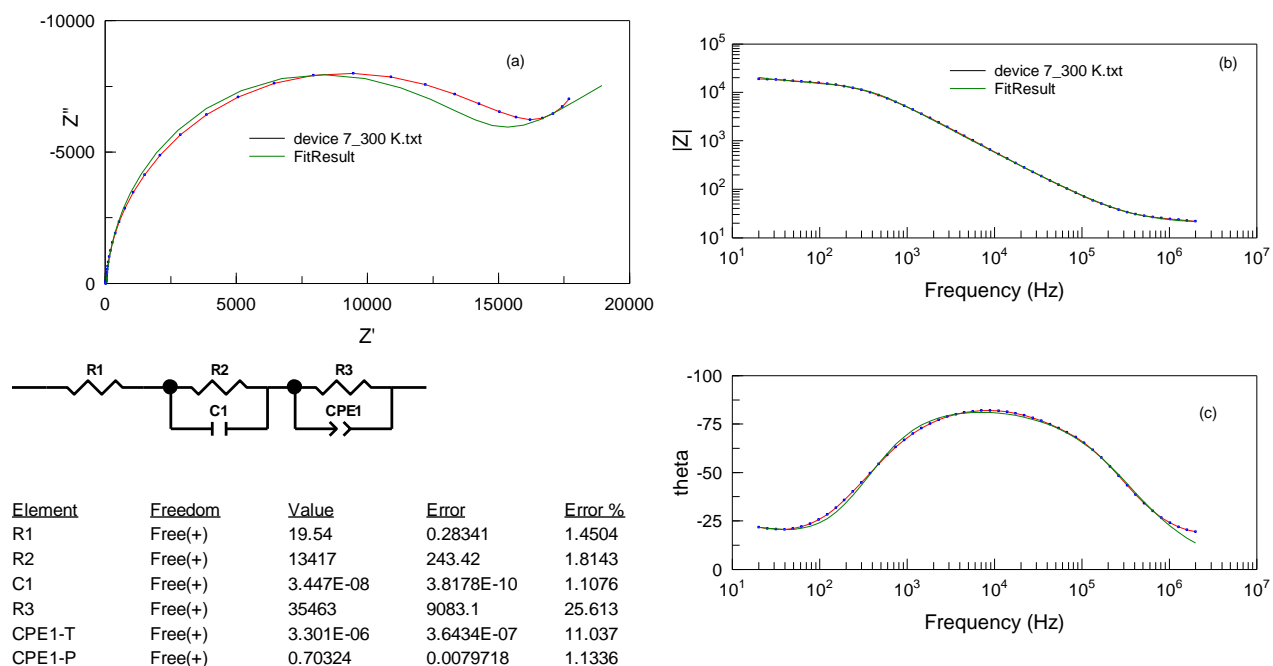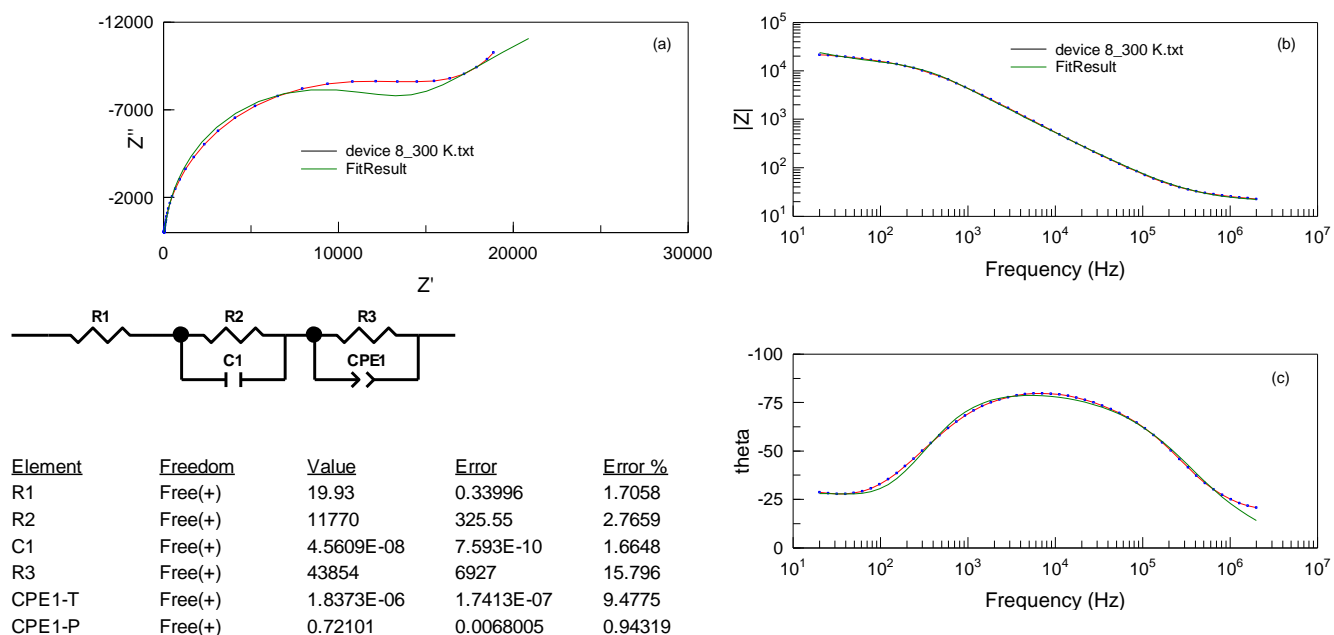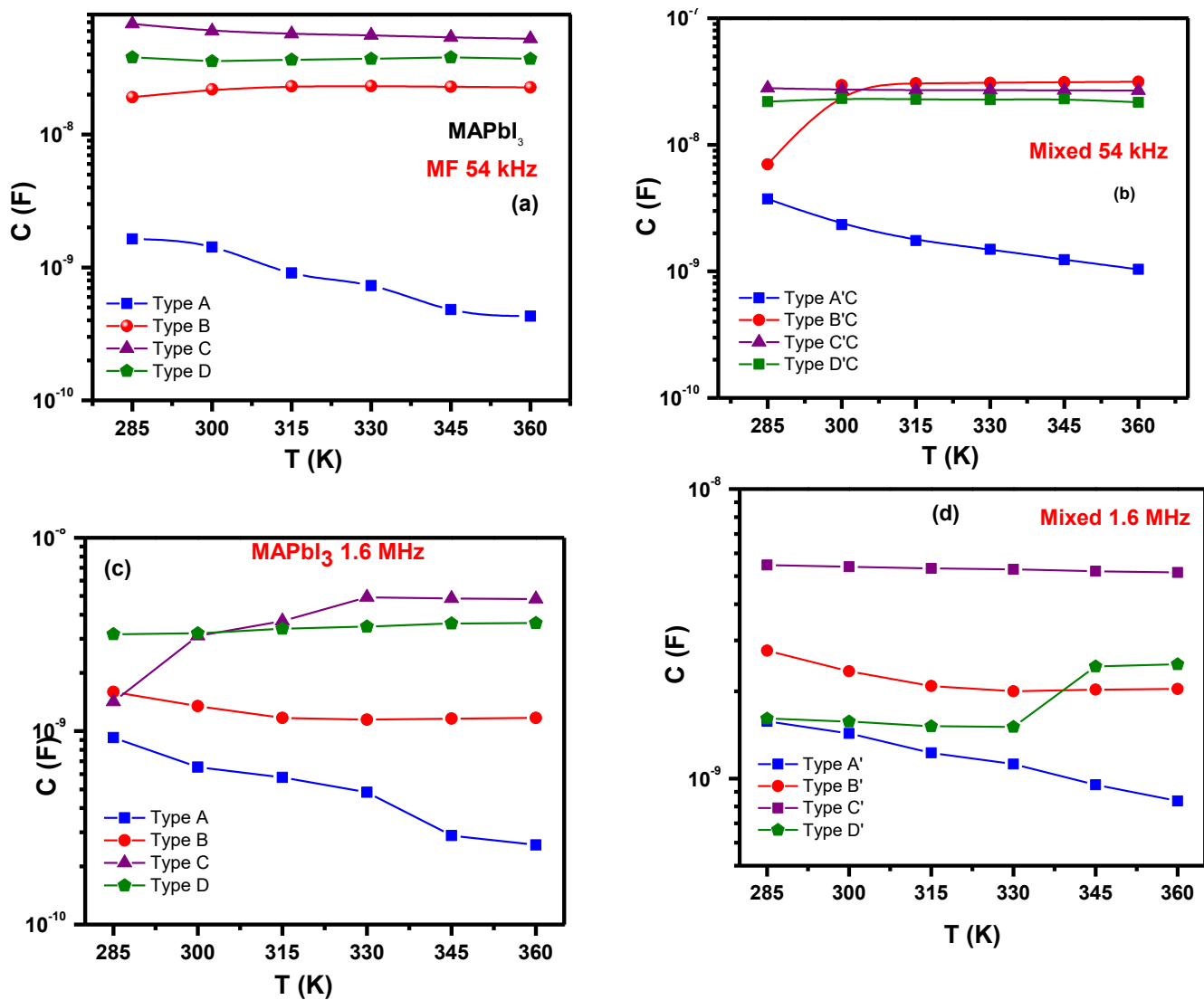| Element	Freedom	Value	Error	Error %
R1	Free(+)	19.93	0.33996	1.7058
R2	Free(+)	11770	325.55	2.7659
C1	Free(+)	4.5609E-08	7.593E-10	1.6648
R3	Free(+)	43854	6927	15.796
CPE1-T	Free(+)	1.8373E-06	1.7413E-07	9.4775
CPE1-P	Free(+)	0.72101	0.0068005	0.94319

Figure S7. Fitting of impedance spectra of Type D' in (a) complex plane and (b and c) Bode plot

Figure S8. Temperature dependence of (a, b) Intermediate frequency and (c, d) high frequency capacitance of all devices.
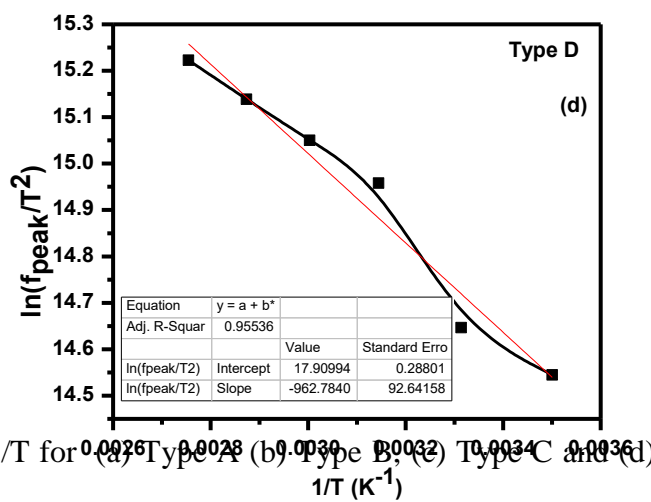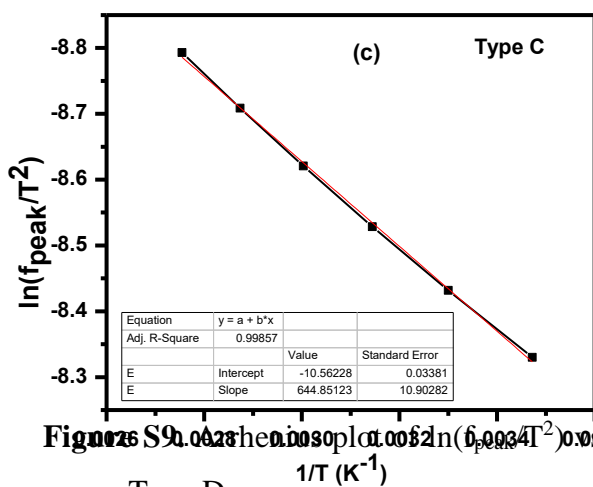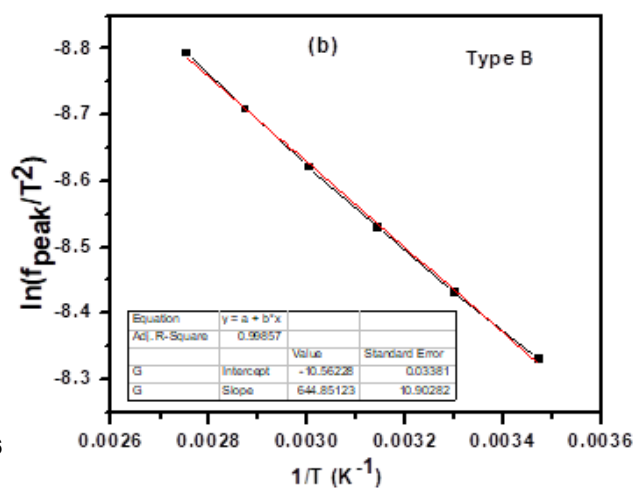
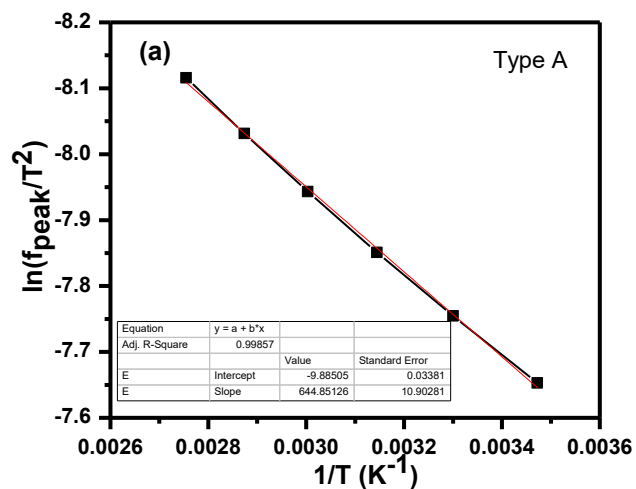## S2. Evaluation of activation energy

(a) Type A

$\ln(f_{peak}/T^2)$ vs $1/T\ (K^{-1})$

Equation	y = a + b*x		
Adj. R-Square	0.99857		
		Value	Standard Error
E	Intercept	-9.88505	0.03381
E	Slope	644.85126	10.90281

(b) Type B

$\ln(f_{peak}/T^2)$ vs $1/T\ (K^{-1})$

Equation	y = a + b*x		
Adj. R-Square	0.99857		
		Value	Standard Error
G	Intercept	-10.56228	0.03381
G	Slope	644.85123	10.90282

(c) Type C

$\ln(f_{peak}/T^2)$ vs $1/T\ (K^{-1})$

Equation	y = a + b*x		
Adj. R-Square	0.99857		
		Value	Standard Error
E	Intercept	-10.56228	0.03381
E	Slope	644.85123	10.90282

(d) Type D

$\ln(f_{peak}/T^2)$ vs $1/T\ (K^{-1})$

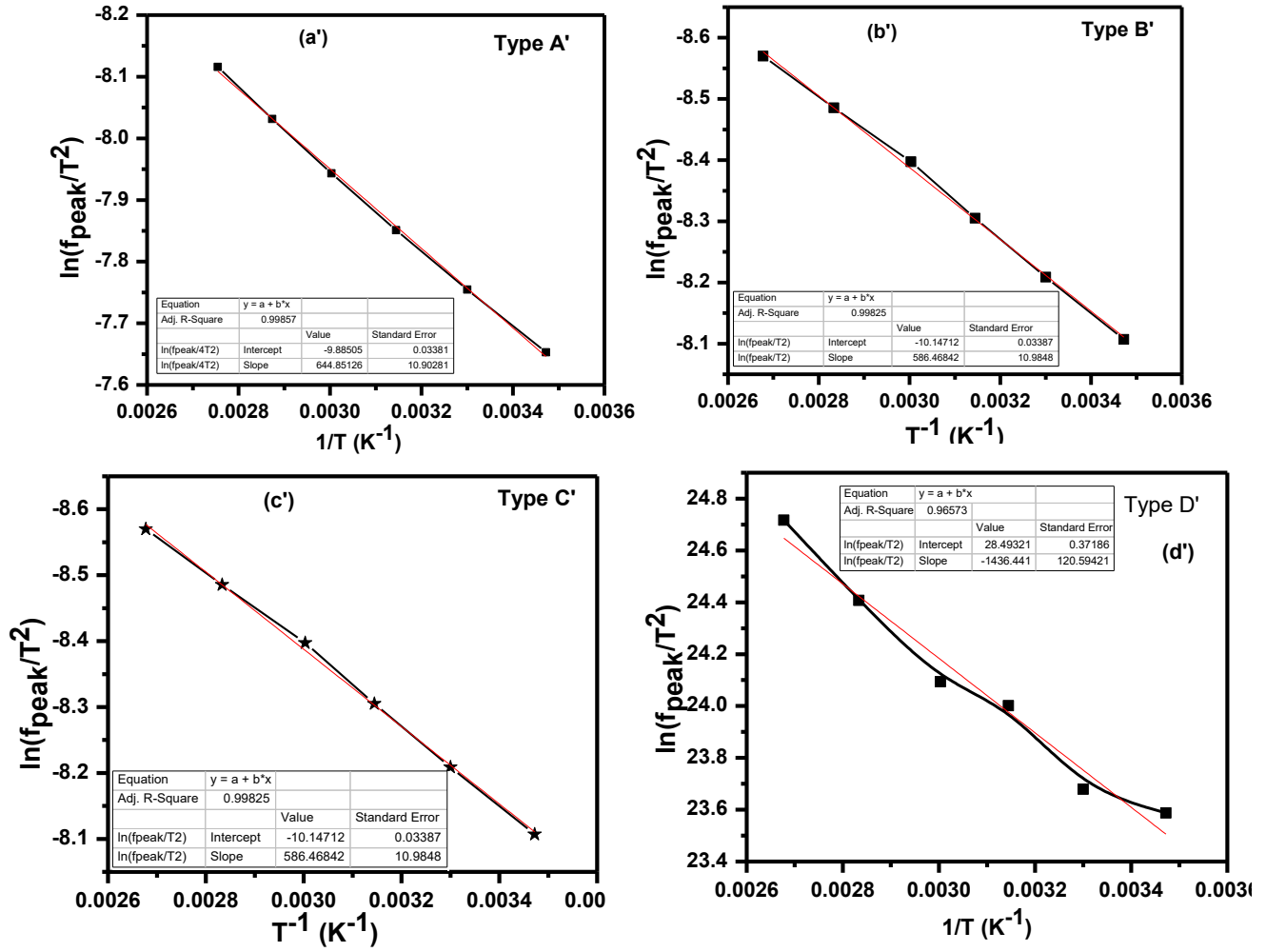| Equation	y = a + b*		
Adj. R-Squar	0.95536		
		Value	Standard Erro
ln(fpeak/T2)	Intercept	17.90994	0.28801
ln(fpeak/T2)	Slope	-962.7840	92.64158

Figure S9. Arrhenius plot of $\ln(f_{peak}/T^2)$ vs $1/T$ for (a) Type A (b) Type B; (c) Type C and (d) Type D.

Figure S10. Arrhenius plot of $\ln(f_{peak}/T^2)$ vs. $1/T$ for (a') Type A' (b') Type B', (c') Type C' and (d') Type D'.

The density of state N_C was estimated from the relation

$$N_C = \frac{\upsilon_o}{v_{th}\sigma_n}$$

where υ_o is attempt to escape frequency (ATEF), v_{th} is the root mean square thermal velocity of

electrons and equal to $v_{th} = \sqrt{\dfrac{3k_B T}{m}} = 1.17 \times 10^7 \, cm/s$ at 300 K, and σ_n is the capture cross section of trap for both electron and hole $\sim 1 \times 10^{-14}$ cm^{-2} [Y. Wang, Z. Xia, J. Liang, X. Wang, Y. Liu, C. Liu, S. Zhang and H. Zhou, Semicond. Sci. Technol. 30 (2015) 054004].

The value of ATEF$^{\upsilon_o}$ was estimated from the relation

$$\upsilon_0 = \xi T^2$$

The intercept of Arrhenius plot, $\ln\left(\dfrac{f_{peak}}{T^2}\right) vs. \dfrac{1}{T}$ shown in above Figures give the value of $\ln(\xi)$.
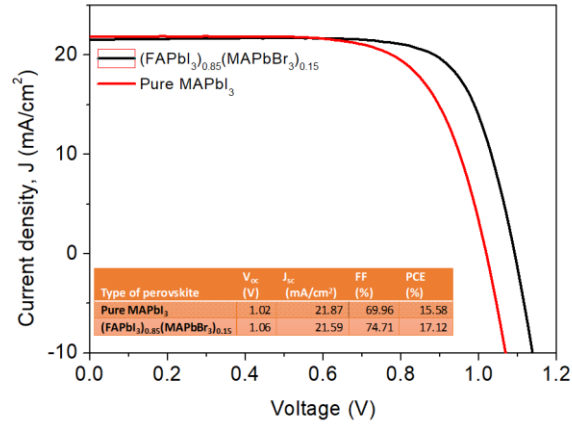

Fig.S11: Representative *J-V* curves for fabricated solar cells.